Smith-Magenis syndrome protein RAI1 regulates body weight homeostasis through hypothalamic BDNF-producing neurons and neurotrophin downstream signalling

Sehrish Javed[1,2], Ya-Ting Chang[1,2], Yoobin Cho[1,2], Yu-Ju Lee[1,2], Hao-Cheng Chang[1,2], Minza Haque[1,2], Yu Cheng Lin[1,2], Wei-Hsiang Huang[1,2,*]

Affiliations:

[1]Department of Neurology and Neurosurgery, Centre for Research in Neuroscience, McGill University, Montréal, QC H3G 1A3, Canada

[2]Brain Repair and Integrative Neuroscience Program, The Research Institute of the McGill University Health Centre, Montréal, QC H3G 1A3, Canada

*Corresponding author. Email: wei-hsiang.huang@mcgill.ca

Abstract

Retinoic acid-induced 1 (*RAI1*) haploinsufficiency causes Smith-Magenis syndrome (SMS), a genetic disorder with symptoms including hyperphagia, hyperlipidemia, severe obesity, and autism phenotypes. RAI1 is a transcriptional regulator with a pan-neural expression pattern and hundreds of downstream targets. The mechanisms linking neural *Rai1* to body weight regulation remain unclear. Here we find that hypothalamic brain-derived neurotrophic factor (BDNF) and its downstream signalling are disrupted in SMS ($Rai1^{+/-}$) mice. Selective *Rai1* loss from all BDNF-producing cells or from BDNF-producing neurons in the paraventricular nucleus of the hypothalamus (PVH) induced obesity in mice. Electrophysiological recordings revealed that *Rai1* ablation decreased the intrinsic excitability of PVH^{BDNF} neurons. Chronic treatment of SMS mice with LM22A-4 engages neurotrophin downstream signalling and delayed obesity onset. This treatment also partially rescued disrupted lipid profiles, insulin intolerance, and stereotypical repetitive behaviour in SMS mice. These data argue that RAI1 regulates body weight and metabolic function through hypothalamic BDNF-producing neurons and that targeting neurotrophin downstream signalling might improve associated SMS phenotypes.

Introduction

Obesity is an increasing global concern: 20% of the world's adult population is expected to become obese by 2025 if current trends persist (Collaboration, 2017). However, the complex environmental, behavioural, and genetic contributions to obesity make this a complex condition to model and address. Monogenic obesity disorders provide a consistent system where the pathophysiology, genetic predisposition, and neurobiology underlying phenotypes can potentially provide insights that translate to polygenic obesity (Loos & Yeo, 2022).

One such monogenic disorder is Smith-Magenis syndrome (SMS; OMIM #182290) (Smith *et al*, 1986), a neurogenetic condition frequently associated with obesity. 80% of SMS cases are caused by interstitial deletions of the 17p11.2 chromosomal region containing a dosage-sensitive gene, *retinoic acid-induced 1* (*RAI1*) (Slager *et al*, 2003). Most SMS patients are overweight (40% > 95th percentile weight, 80% > 85th percentile weight) and exhibit over-eating tendencies by adolescence (Alaimo *et al*, 2015; Burns *et al*, 2010; Gandhi *et al*, 2022). 20% of SMS patients do not have 17p11.2 deletions but instead carry *RAI1* point mutations that are still frequently associated with obesity (Boot *et al*, 2021; Edelman *et al*, 2007). These clinical data indicate that RAI is critical for body weight regulation.

The human RAI1 protein shares >80% sequence identity with the mouse RAI1 protein, allowing us to study RAI1 function *in vivo* (Huang *et al*, 2016; Javed *et al*, 2020). We previously found that *Rai1* encodes a transcriptional regulator that binds to the promoter or enhancer regions of its target genes, most of which are involved in neurodevelopment and synaptic transmission (Huang *et al.*, 2016). SMS (*Rai1*$^{+/-}$) mice exhibit obesity associated with hyperphagia and increased adiposity (Burns *et al.*, 2010; Huang *et al.*, 2016). Interestingly, RAI1 may have a sexually

60 dimorphic function, as female SMS mice exhibit more pronounced obesity than males (Burns *et*
61 *al.*, 2010; Huang *et al.*, 2016).

62 Using a homozygous *Rai1* conditional knockout (*Rai1*-cKO) mice, we found that *Rai1* deletion
63 in either subcortical excitatory neurons (vGlut2$^+$) or single-minded homolog 1 (Sim1$^+$) neurons
64 induced obesity in mice (Huang *et al.*, 2016). Sim1$^+$ neurons reside in several brain regions
65 including the nucleus of the lateral olfactory tract, the supraoptic nucleus, the medial amygdala,
66 and the paraventricular nucleus of the hypothalamus (PVH), a region that is critical for body
67 weight regulation (Balthasar *et al*, 2005). Sim1$^+$ neurons in the PVH are composed of several
68 molecularly defined cell types, including those that express oxytocin, vasopressin, corticotropin-
69 releasing hormone, somatostatin, melanocortin-4-receptor (MC4R), growth hormone-releasing
70 hormone (GHRH), or brain-derived neurotrophic factor (BDNF) (An *et al*, 2015). Deleting *Bdnf*
71 from the PVH results in obesity due to increased food intake, reduced energy expenditure, and
72 reduced locomotion (An *et al.*, 2015). While PVH neuronal activity is reduced during feeding
73 (Xu *et al*, 2019), activation of PVH^{BDNF} neurons results in weight loss (Wu & Xu, 2022). We
74 recently found that RAI1 promotes *Bdnf* expression in the hypothalamus throughout life (Javed
75 *et al*, 2021). We hypothesized that RAI11 may be connected to BDNF-producing neurons in
76 PVH, explaining how a neural transcription factor regulates body weight homeostasis.

77 BDNF regulates energy metabolism by binding to its cognate receptor tropomyosin receptor
78 kinase B (TRKB) (An *et al.*, 2015) and may thus provide a potential therapeutic target for SMS.
79 However, the link between *RAI1, BDNF*, and SMS symptoms is unclear. Patients carrying
80 monogenic mutations in either *BDNF* (Gray *et al*, 2006) or *NTRK2* (encoding TRKB) (Yeo *et al*,
81 2004) experience severe hyperphagic obesity. Moreover, obesity and associated metabolic
82 dysfunctions such as impaired glucose and insulin sensitivity are correlated with impaired PI3K-

83 AKT pathway, a TRKB downstream target (Su *et al*, 2021). Given that (1) *Bdnf* overexpression
84 during early embryonic development or (2) targeting *Bdnf* overexpression to the PVH of
85 adolescent SMS (*Rai1*$^{+/-}$) mice protected them from weight gain and metabolic defects (Javed *et*
86 *al.*, 2021), and that (3) a point mutation in *RAI1* disrupts its ability to transcriptionally enhance
87 *BDNF* expression *in vitro* (Abad *et al*, 2018), pharmacological targeting of neurotrophin
88 downstream signalling is an attractive and yet unexplored therapeutic avenue for SMS.

89 Building on our previous discoveries, here we examine the neurobiological functions of RAI1 in
90 BDNF-producing neurons, specifically those that reside in the PVH. Importantly, we evaluated
91 the involvement of the BDNF-TRKB pathways in SMS pathogenesis using a small molecule
92 drug (LM22A-4) to enhance neurotrophin downstream signalling. Our work indicates that
93 PVH^{BDNF} neurons depend on RAI1 to maintain normal neuronal activity and regulate body
94 weight homeostasis, and dysfunction of BDNF downstream signalling contributes to obesity
95 associated with SMS mice.

96

Results

Rai1 deficiency dysregulates specific downstream targets of neurotrophin in the mouse hypothalamus

Multiple lines of evidence indicated that SMS mice show decreased *Bdnf* mRNA expression in the hypothalamus (Burns *et al.*, 2010; Huang *et al.*, 2016; Javed *et al.*, 2021). To determine if BDNF protein levels were consequently altered in the hypothalamus, we performed an enzyme-linked immunosorbent assay (ELISA) and found that BDNF protein levels were significantly reduced in 7-week-old pre-symptomatic SMS mice relative to controls (**Fig 1A**). To quantify if molecular pathways associated with BDNF downstream signalling were altered, we subjected hypothalamic tissue lysates from 7-week-old pre-obese SMS and control (Ctrl) mice to reverse phase protein array (RPPA) (**Fig 1B**). Control and SMS samples are clustered separately in the principal component analysis (**Fig 1C**).

Hierarchical clustering analysis indicated that most differentially expressed phosphorylated proteins (**Fig 1D**) and total proteins (**Figure 1—figure supplement 1**) were downregulated in SMS mice. We mapped total proteins, as well as phospho-proteins, that were differentially expressed in Ctrl and SMS samples onto the interconnected biological network and identified a subset of connected nodes downregulated in SMS (FDR < 10e-5) belong to the neurotrophin, PI3K-AKT, and mTOR signalling cascades (**Fig 1E**). These molecules are known to play a critical role in regulating body weight homeostasis and can be activated by BDNF either directly (neurotrophin pathway) or indirectly (PI3K-AKT and mTOR pathways) (Cota *et al*, 2006; Schultze *et al*, 2012). The expression levels of PIK3CA, a common node in these pathways, were significantly reduced in the SMS mice compared to controls (**Fig 1F**). Moreover, the expression levels of phosphorylated NF-κB (nuclear factor-kappa B), a downstream target of the

neurotrophin pathway, were significantly reduced in the SMS group (**Fig 1G**). Together, these results suggest that *Rai1* loss impairs specific pathways, including neurotrophin signalling, and indicate that dysfunction of BDNF-producing cells could contribute to SMS pathogenesis.

BDNF-producing cells depend on RAI1 to regulate body weight homeostasis

To target BDNF-producing cells, we used a *Bdnf*$^{Cre/+}$ mouse line that carries a viral 2A oligopeptide and Cre recombinase immediately upstream of *Bdnf*'s endogenous STOP codon (Tan *et al*, 2016). We crossed the *Bdnf*$^{Cre/+}$ mice with tdTomato-Ai9 reporter mice and found that Ai9 signals faithfully reflected endogenous BDNF protein expression in the PVH (**Figure 2—figure supplement 1A-E**). We also found that RAI1 is expressed in PVH^{BDNF} cells that are distinct from larger magnocellular cells, such as the PVH oxytocin neurons (**Figure 2—figure supplement 2A-I**). Specifically, 55% of PVH^{BDNF} neurons express RAI1, whereas only 2% of PVH^{Oxytocin} neurons express RAI1 (**Figure 2—figure supplement 2I**). These data suggest that RAI1 is enriched in BDNF-producing neurons in the mouse PVH.

To determine if BDNF-producing cells depend on RAI1 to regulate body weight, we deleted one or both copies of *Rai1* using the *Bdnf*$^{Cre/+}$ and the conditional *Rai1*$^{fl/fl}$ mice (Huang *et al.*, 2016) (**Fig 2A, Figure 2—figure supplement 3A**). Conditional knockout mice (cKO: *Bdnf*$^{Cre/+}$*;* *Rai1*$^{fl/fl}$) showed a significant reduction in Rai1 expression in PVH^{BDNF} neurons compared to controls (**Fig 2B-C**, **Figure 2—figure supplement 3B)**. The total number of BDNF-producing cells in the PVH remained similar in Ctrl and cKO mice (**Figure 2—figure supplement 3C**), indicating that RAI1 loss did not affect PVH neurogenesis or survival.

We monitored body weight weekly and found that male and female cKO mice showed a significant increase in body weight beginning at 15 weeks of age compared to controls (Ctrl: *Bdnf*$^{Cre/+}$) (**Fig 2D**, **Figure 2—figure supplement 4A**). However, conditional *Rai1* heterozygous mice (*Bdnf*$^{Cre/+}$*; Rai1*$^{fl/+}$) did not show a pathological increase in body weight (**Figure 2—figure supplement 3D**, **Figure 2—figure supplement 4B**), suggesting that non-BDNF-producing cells also contribute to SMS pathogenesis. EcoMRI found that 26-week-old cKO male and female mice showed increased fat mass but not lean mass (**Fig 2E**, **Figure 2—figure supplement 4C**). Further dissection of fat tissues from different organs showed an increased mass of subcutaneous inguinal (S.C. Ing.) fat in cKO mice of both sexes and an increased mass of epididymal adipose tissues (eWAT) in female cKOs (**Fig 2F**, **Figure 2—figure supplement 4D**).

In contrast, the total mass of brown adipose tissue (BAT) remained unchanged between groups (**Fig 2F**, **Figure 2—figure supplement 4D**). In both male and female cKO mice, we found hypertrophic eWAT adipocytes (**Fig 2G**, **Figure 2—figure supplement 4E**) and elevated blood leptin levels (**Fig 2H**, **Figure 2—figure supplement 4F**). However, there was no significant alteration in blood lipids such as triglycerides (TG), high-density lipoprotein (HDL), low-density lipoproteins (LDL), and very low-density lipoprotein (VLDL) in either male or female cKO mice (**Figure 2—figure supplement 3E-G**, **Figure 2—figure supplement 4G-I)**. These data suggest that obesity caused by ablating *Rai1* from BDNF-producing cells is associated with increased fat mass, fat deposition, and leptin levels.

Obesity could result from increased food intake, reduced energy expenditure, or both. Similar to SMS mice, male and female cKO mice did not have defects in respiratory exchange rates when measured by indirect calorimetry (**Figure 2—figure supplement 3H**, **Figure 2—figure supplement 4J**). Interestingly, cKO mice showed sex-specific differences in energy expenditure.

During the dark phase, female cKO mice showed reduced energy expenditure (Fig 2I) and decreased total locomotor activity (**Fig 2J**). In contrast, total food intake remained unchanged (**Fig 2K**). Male cKO mice became hyperphagic (**Figure 2—figure supplement 4K**), showed increased energy expenditure during the dark phase (**Figure 2—figure supplement 4L**), and exhibited normal locomotor activity when compared to controls (**Figure 2—figure supplement 4M**). These results suggest that obesity in male cKO mice is attributable to overeating despite increased energy expenditure.

To determine if *Rai1* loss from BDNF-producing cells impacts metabolic function, a glucose tolerance test (GTT) was performed. Interestingly, cKO mice of both sexes showed normal blood glucose levels right before the test but became hyperglycemic 20 minutes (female cKO) and 45 minutes (male cKO) after glucose administration (**Fig 2L**, **Figure 2—figure supplement 4N**). This change was accompanied by a significantly higher area under the curve (AUC) for both groups (**Figure 2—figure supplement 3I**, **Figure 2—figure supplement 4O**). While the male cKO mice remained hyperglycemic throughout the GTT (**Figure 2—figure supplement 4N**), the glucose levels in female cKO mice returned to normal towards the end (**Fig 2L**). We also found increased blood insulin levels during the GTT in both sexes (**Figure 2—figure supplement 3J**, **Figure 2—figure supplement 4P**). In the insulin tolerance test (ITT), female cKO mice showed moderately elevated glucose levels 20 minutes into the test (**Figure 2—figure supplement 3K**). By contrast, male cKO mice showed considerably higher glucose levels than controls in the ITT (~6.5 ng/ml for cKO and ~2.0ng/ml for Ctrl) during the 60- to 120-minute intervals (**Figure 2—figure supplement 4Q**). These experiments demonstrate that BDNF-producing cells depend on RAI1 to regulate body weight, adiposity, glucose and insulin tolerance in mice.

Rai1 deletion reduces PVH^{BDNF} neuronal excitability

BDNF-producing neurons are widely distributed in the hypothalamus, being found in the dorsomedial hypothalamus (Unger *et al*, 2007), ventromedial hypothalamus (Xu *et al*, 2003), and PVH (An *et al.*, 2015). To understand how *Rai1* loss affects intrinsic neuronal excitability and synaptic transmission of PVH^{BDNF} neurons that underlie energy homeostasis (An *et al.*, 2015), we fluorescently labelled them with Cre-dependent tdTomato (**Fig. 3A**). We found that a hyperpolarized step followed by increasing the holding voltage at resting membrane potentials (Rm) was able to initiate rebound firing or rebound repetitive firing in most PVH^{BDNF} neurons (**Figure 3—figure supplement 1A**). Hyperpolarization-induced I_H currents and low depolarization events were observed in some PVH^{BDNF} neurons (**Figure 3—figure supplement 1A**). cKO PVH^{BDNF} neurons showed reduced action potential (AP) firing frequency at a holding voltage of -60mV compared to Ctrl PVH^{BDNF} neurons (**Fig 3B-C**). The resting membrane potential (Rm) of cKO (-52mV) neurons showed a 10mV positive shift compared to Ctrl neurons (-62mV) (**Fig 3D**). We also found that fewer cKO PVH^{BDNF} neurons showed spontaneous firing at Rm (**Fig 3E**, Ctrl:10/13; cKO:5/12) and at a holding voltage of -70mV (**Fig 3F**, Ctrl:6/12; cKO:1/12) compared to Ctrl PVH^{BDNF} neurons. The threshold of the first AP initiated by a ramp current injection (1 nA/sec) from Rm was significantly increased in cKO neurons (**Fig 3G-H**). Because a wider shoulder and lower AP amplitude were observed when held at more depolarized potentials (**Figure 3—figure supplement 1B**), we compared the AP waveforms at a holding voltage of -60mV, close to the Rm of both genotypes. The AP of the cKO group exhibited a lower peak amplitude (measuring from the threshold to peak) (**Fig 3I**), a normal threshold (**Fig 3J**), and a normal half-width (**Figure 3—figure supplement 1C**). In summary, we found that both passive and AP properties of cKO PVH^{BDNF} neurons were altered due to RAI1 loss. The

Rm of cKO neurons shifted to a more positive voltage than the gating threshold of voltage-gated sodium channels (6/12 were more positive than -55mV), which was unfavourable for their transition from the inactivation state to the closed state. Combined with the higher AP threshold of cKO neurons, these changes contribute to a decreased excitability in cKO PVH^{BDNF} neurons.

PVN neurons receive glutamatergic and GABAergic inputs and are tonically inhibited by GABAergic neurons (Colmers & Bains, 2018; Gao *et al*, 2017). We observed a slight rightward shift of the probability of miniature inhibitory postsynaptic current (mIPSC) frequency in cKO PVH^{BDNF} neurons, although the average frequency (**Fig 3K**) was not significantly different between groups. The probability of mIPSC amplitude also showed a right shift without a significant change (**Fig 3L, Figure 3—figure supplement 1D**). However, we observed a significantly increased area under the curve (**Fig 3M**). Interestingly, we found that cKO PVH^{BDNF} neurons had a smaller cellular diameter (**Figure 3—figure supplement 1E**). Overall, our data argue that *Rai1* deletion decreases the excitability and AP firing of PVH^{BDNF} neurons without significant changes in synaptic inhibitory transmission.

RAI1 is necessary for PVH^{BDNF} neurons to regulate energy homeostasis

Reduced PVH^{BDNF} neuronal activity in cKO mice suggested that RAI1 loss in BDNF-producing PVH neurons might be sufficient to induce defective energy homeostasis *in vivo*. To test this hypothesis by deleting *Rai1* only in PVH^{BDNF} neurons but not other BDNF-producing cells, we performed PVH^{BDNF}-specific *Rai1* deletion using a CRISPR/Cas9 system packaged into AAV9. Two viruses were delivered: one encoding a reporter molecule (GFP) and three single guide RNAs targeting the *Rai1* gene (sgRai1), and the other carrying Cre-dependent *Staphylococcus aureus* CRISPR-associated protein 9 (saCas9) (**Fig 4A**). Hereafter, our experiments focus on

female SMS mice since they showed more consistent defects in fat distribution (Burns *et al.*, 2010) and body weight regulation (Huang *et al.*, 2016) than males. Bilateral administration of two AAVs into the PVH of female *Bdnf*$^{Cre/+}$ mice (Exp group) at 3 weeks of age resulted in a significant loss of Rai1 protein expression in PVH^{BDNF} neurons when compared to *Bdnf*$^{Cre/+}$ mice injected with an AAV encoding the *sgRai1* and GFP (Ctrl group) (**Fig 4B-C**, **Figure 4—figure supplement 1A**). Quantification of AAV-infected (GFP^{+}) BDNF neurons showed that while the total number of BDNF^{+} (**Figure 4—figure supplement 1B**) and BDNF^{+} GFP^{+} (**Figure 4—figure supplement 1C**) cells were not different in the two groups, the percentage of AAV-infected BDNF^{+} cells that express RAI1 was significantly reduced in the Exp group (**Fig 4C**, **Figure 4—figure supplement 1D-E**). Moreover, the virus expression did not spread to the non-PVH neighboring nuclei (**Figure 4—figure supplement 1F**). Deleting *Rai1* from the PVH^{BDNF} neurons resulted in a significant increase in body weight beginning at 17 weeks of age (**Fig 4D**). Similar to the cKO (*Bdnf*$^{Cre/+}$*; Rai1*$^{fl/fl}$) mice, obesity in 26-week-old Exp mice was due to increased fat mass (**Fig 4E**) and more specifically, increased subcutaneous inguinal (S.C. ing) and epididymal white adipose tissues (eWAT) but not BAT (**Fig 4F**). We also found that eWAT adipocytes became hypertrophic (**Fig 4G**). Similar to the cKO mice, food intake did not differ between Exp and Ctrl groups (**Fig 4H**), likely due to the high level of satiety signals in the brain caused by increased blood leptin levels (**Fig 4I**). We also found that energy expenditure (**Fig 4J**), respiratory exchange rate (**Figure 4—figure supplement 1G**), and blood lipid parameters, including TG (**Figure 4—figure supplement 1H**), HDL (**Figure 4—figure supplement 1I**), LDL and VLDL levels (**Figure 4—figure supplement 1J**), were similar in Exp and Ctrl groups, consistent with the cKO data (**Figure 2**). Interestingly, Exp mice showed significantly less locomotor activity during the dark phase than the Ctrl mice (**Fig 4K**). A GTT indicated that Exp

mice have a hyperglycemic profile (**Fig 4L**), accompanied by a slightly higher area under the curve for blood glucose levels (p=0.05) (**Fig 4M**). Insulin levels in Exp mice were also significantly elevated 15 minutes after glucose administration (**Fig 4N**).

While Exp mice showed a trend towards increased glucose levels in insulin tolerance tests, the change was not statistically different (**Figure 4—figure supplement 1K**). Altogether, these experiments indicate that conditional deletion of *Rai1* from PVH^{BDNF} neurons during adolescence impairs the regulation of body weight, adiposity, glucose tolerance, and locomotion. These changes recapitulate most phenotypes observed in cKO mice with *Rai1* deleted in BDNF-producing cells from early development.

Pharmacologically enhancing neurotrophin downstream signalling partially alleviates obesity in SMS mice

Our findings so far indicate that multiple pathways, including neurotrophin signalling, are dysregulated in SMS mice, and that Rai1 loss from BDNF-producing cells, including PVH^{BDNF} neurons, impairs energy homeostasis *in vivo*. Next we sought to examine the contribution of BDNF dysfunction in SMS pathogenesis by pharmacologically activating downstream targets of the neurotrophin pathway.

We systematically treated mice with LM22A-4, a potential small molecule BDNF loop domain mimetic (Massa *et al*, 2010). To measure the bioavailability of LM22A-4 in the SMS brain, we simultaneously administered LM22A-4 intranasally (5 mg/kg body weight) and intraperitoneally (50 mg/kg body weight), using the highest doses used in previous studies (Canals *et al*, 2004; Chang *et al*, 2006; Gu *et al*, 2022; Kron *et al*, 2012; Ogier *et al*, 2007). We then harvested

forebrain and hypothalamic tissues one or three hours after drug administration. The spectrometric analysis found a significantly higher LM22A-4 concentration in both brain regions one-hour post-treatment, while its concentration decreased three hours after treatment (**Figure 5—figure supplement 1A**). Consistent with the reduced neurotrophin signalling observed in our proteomic analysis, saline-treated SMS mice showed reduced phosphorylated-AKT (p-AKT; **Fig 5A**, **Figure 5—figure supplement 1B**, **Figure 5—source data 1, Figure 5—figure supplement 1 source data 1**) levels in the hypothalamus. LM22A-4 treatment significantly increased the levels of p-AKT in the SMS mice 1-hr post-treatment (**Fig 5A**, **Figure 5—figure supplement 1B**, **Figure 5—source data 1**, **Figure 5—figure supplement 1 source data 1**), indicating increased signalling downstream of the BDNF pathway.

We next examined if chronic LM22A-4 treatment was sufficient to reverse or modify the progression of the obesity phenotype in adult SMS mice. Specifically, we treated SMS mice daily from 8 to 14 weeks of age, during which SMS mice began to gain significantly more weight. Saline-treated SMS mice (**Fig 5C**) were significantly heavier than saline-treated control mice from 9 weeks of age onward. Interestingly, LM22A-4-treated SMS mice showed a similar body weight to saline-treated control littermates until 13 weeks of age but became obese by 14 weeks of age (**Fig 5D**). Consistent with a partial rescue, LM22A-4-treated SMS mice were significantly less obese than saline-treated SMS mice throughout the treatment period (**Fig 5E**). Control mice treated with LM22A-4 did not show a further reduction in body weight (**Figure 5—figure supplement 1C**), indicating that the therapeutic effects were specific to SMS pathogenesis.

We measured food intake and found that LM22A-4 did not significantly rescue increased food intake in SMS mice (**Fig 5F**). SMS mice showed normal energy expenditure (**Figure 5—figure**

supplement 1D) and respiratory exchange rate (**Figure 5—figure supplement 1E**), neither of which was altered by LM22A-4 treatment. Interestingly, we did observe a partial rescue of locomotor activity in LM22A-4-treated SMS mice that was not significantly different from saline-treated Ctrl or SMS mice (**Fig 5G**). We also found that the LM22A-4 treatment partially rescued fat deposition (**Fig 5H**) and completely rescued HDL levels (**Fig 5I**) in SMS mice. During an insulin tolerance test, we found that saline-treated SMS mice showed increased baseline insulin levels (**Fig 5J**) and blood glucose levels during the test (**Fig 5K**), both of which were partially rescued by LM22A-4 treatment.

In addition to a deficit in energy homeostasis, SMS mice showed two highly reproducible behavioural deficits: increased stereotypic rearing in the open field and decreased social dominance in the tube test (Huang *et al*, 2018; Rao *et al*, 2017). Saline-treated SMS mice showed significantly more rearing behaviour when compared to the saline-treated controls (**Fig 5L**). Interestingly, the LM22A-4 treatment reduced the repetitive rearing behaviour in SMS mice **(Fig 5L**). LM22A-4 treatment did not change repetitive behaviours in control mice (**Figure 5—figure supplement 1F**), suggesting the effect is specific to *Rai1* haploinsufficiency. However, we did not observe a rescue of social dominance deficits in SMS mice (**Figure 5—figure supplement 2A-E**). Together, these data indicate that LM22A-4 treatment delayed the onset of obesity and fully rescued repetitive behaviour in SMS mice, suggesting that neurotrophin downstream signalling dysfunction contributes to changes in the mouse SMS brain linked to obesity and behavioural phenotypes.

Discussion

The hypothalamus and neurotrophin signalling in this region control body weight by regulating the intricate balance between energy intake and expenditure (Xu & Xie, 2016). The role of BDNF-producing neurons in human obesity disorders and how the activity of these cells is regulated remained poorly studied. We found that *Rai1* deficiency, linked to Smith-Magenis syndrome (SMS), regulates BDNF expression and maintains intrinsic excitability in PVH^{BDNF} neurons.

Consistent with this mechanism, we found that removing RAI1 from BDNF-producing neurons or PVH^{BDNF} neurons results in imbalanced energy homeostasis and obesity. A small molecule drug LM22A-4 led to increased AKT phosphorylation and partially rescued locomotor activity, insulin intolerance, and HDL levels, while delaying the onset of obesity in SMS mice. These findings highlight a potential role for hypothalamic BDNF-producing neurons, specifically PVH^{BDNF} neurons, in SMS pathogenesis and highlight BDNF signalling as a potentially druggable pathway to improve energy homeostasis defects and repetitive behaviours commonly observed in SMS patients (Burns *et al.*, 2010; Moss *et al*, 2009).

The involvement of different PVH subtypes in human obesity is only beginning to be elucidated. Dysfunction of oxytocin PVH neurons is linked to the Prader-Willi syndrome (Lee *et al*, 2012), another genetic disorder associated with obesity. Since *Rai1* expression is enriched in PVH^{BDNF} neurons but not $PVH^{Oxytocin}$ neurons, our data suggest that distinct pathophysiological mechanisms underlie SMS and Prader-Willi syndrome.

The conditional knockout analysis allowed us to precisely map the cell-specific origin of neuropathological phenotypes, such as SMS-like symptoms in mice. Our previous work found that deleting *Rai1* from cortical excitatory neurons using an $Emx1^{Cre}$ allele (Gorski *et al*, 2002), from the GABAergic neurons using a $Gad2^{Cre}$ allele (Taniguchi *et al*, 2011), or from astrocytes

using a *Gfap*^{Cre} allele (Garcia *et al*, 2004) did not induce SMS-like obesity (Huang *et al.*, 2016). In contrast, obesity could be induced by ablating *Rai1* from Sim1-lineage neurons and, to a lesser extent, SF1-lineage neurons (Huang *et al.*, 2016). This analysis suggests that Rai1 expression in PVH is more important than in the ventromedial nucleus of the hypothalamus (VMH) for body weight regulation. Interestingly, Although BDNF is required in the VMH and DMH to regulate body weight (Unger *et al.*, 2007), embryonic deletion of *Bdnf* from the SF1-lineage populations including the VMH did not result in obesity (Kamitakahara *et al*, 2016; Yang *et al*, 2016). By contrast, deleting *Bdnf* from Sim1-lineage neurons including the PVH resulted in a more severe obesity phenotype (An *et al.*, 2015). This is consistent with the idea that BDNF expression in PVH is critical for energy homeostasis. We found that *Rai1* expression in BDNF-producing cells regulates energy homeostasis in a sexually dimorphic manner. Specifically, female cKO mice showed normal food intake, decreased energy expenditure, and reduced locomotor activity. In contrast, male cKO mice showed increased food intake with no changes in locomotor activity. Intriguingly, energy expenditure was increased in male cKO mice, likely due to the higher demand to maintain normal activity levels in obese mice. In both sexes, cKO mice showed an increased fat mass and adiposity with no change in lean mass, highlighting an essential role for Rai1 in regulating fat deposition. Our data also indicate that BDNF-producing cells are only partially responsible for obesity in SMS: male and female cKO mice become overweight by 15 weeks, in contrast to SMS mice which become obese by 9 weeks of age, suggesting that non-BDNF neurons contribute to SMS phenotypes.

Notably, mice lacking one copy of *Rai1* in the BDNF-producing cells do not exhibit obesity, whereas SMS patients and SMS mice show pronounced obesity (Burns *et al.*, 2010; Huang *et al.*, 2016; Smith *et al*, 2005). This indicates that although reduced *Bdnf* expression and

BDNF-producing neurons contribute to regulating body weight, additional molecular changes and other hypothalamic populations also play important roles in regulating body weight homeostasis in SMS. Our RPPA data suggest that mTOR signalling is also misregulated in addition to the reduced activation of the neurotrophin downstream cascades. Hypothalamic mTORC1 is crucial to regulate glucose release from the liver, peripheral lipid metabolism, and insulin sensitivity (Burke *et al*, 2017; Caron *et al*, 2016; Smith *et al*, 2015), while mTORC2 regulates glucose tolerance and fat mass (Kocalis *et al*, 2014). How the impaired mTOR signalling contributes to energy homeostasis defects in SMS and the therapeutic potential of targeting this pathway to treat SMS-related obesity remains unclear and warrants future investigation.

What additional RAI1-dependent hypothalamic cell types residing in brain regions other than PVH regulate obesity in SMS? Other important cell types such as TRKB neurons within the PVH (An *et al*, 2020) and several RAI1-expressing hypothalamic nuclei including the arcuate nucleus, ventromedial nucleus of the hypothalamus (VMH), and lateral hypothalamus all play important roles in regulating energy homeostasis. POMC- and AGRP-expressing neurons within the arcuate nucleus are known to regulate food intake and glucose and insulin homeostasis (Quarta *et al*, 2021; Vohra *et al*, 2022). Therefore, *Rai1* function in these neurons could contribute to obesity in SMS, a topic that awaits future investigation.

We found the metabolic phenotypes induced by deleting *Rai1* from BDNF-producing cells were specifically due to *Rai1* deletion in PVH^{BDNF} neurons. Therefore, our study focused on PVH^{BDNF} neurons. Electrophysiological experiments showed that most wild-type PVH^{BDNF} neurons display high-frequency spontaneous AP firing (1-10 Hz) at the resting membrane potential. Most PVH^{BDNF} neurons fire sharp APs held at a hyperpolarized potential and show repetitive

overshoot during the current ramp test. Loss of *Rai1* significantly reduced the intrinsic neuronal excitability of PVH^{BDNF} neurons. Because GABAergic *Rai1* loss did not induce obesity (Huang *et al.*, 2016) and most BDNF-producing neurons are glutamatergic (Canals *et al*, 2001). The ionic changes in PVH^{BDNF} neurons that precisely explain these excitability changes await future investigations. Different groups of PVH neurons show phasic bursting or slowly inactivating delayed rectifier potassium conductance, which are properties mediated by different potassium channels (Lee *et al.*, 2012). Given that our previous RNA-seq experiment found that hypothalamic Rai1 loss induces misexpression of potassium channel subunits *Kcnc2* and *Kcnj11* (Huang *et al.*, 2016), RAI1-dependent potassium channels are likely involved in altered neuronal activity. Furthermore, we found fewer low threshold depolarization events in cKO PVH^{BDNF} neurons during the hyperpolarized voltage step, suggesting a potential involvement of HCN channels.

Our previous work found that *Rai1* loss in the dentate gyrus resulted in neuronal hyperexcitability (Chang *et al*, 2022b). Here we demonstrated that *Rai1* loss in the hypothalamus resulted in neuronal hypoactivity, suggesting that RAI1 regulates neuronal excitability in a cell type-specific manner. Reduced PVH^{BDNF} neuronal activity upon *Rai1* loss could potentially explain obesity, consistent with a previous report that found chemogenetic activation of PVH^{BDNF} neurons promotes negative energy balance by decreasing feeding and increasing energy expenditure (Wu & Xu, 2022).

It is plausible that RAI1 regulates the expression of genes encoding inward rectifier K^+ channels, which regulate neuronal activity and potentially energy homeostasis. For instance, KIR6 (a family of ATP-sensitive potassium channels, K_{ATP}) is widely expressed in the hypothalamus. Deleting the hypothalamic KIR6.2 subunit impairs K_{ATP} channel function and glucose tolerance

(Miki *et al*, 2001; Parton *et al*, 2007). Moreover, reduced expression of hypothalamic GIRK4 (encoding an inwardly rectifying potassium channel) causes obesity (Perry *et al*, 2008). GABAergic neurotransmission from arcuate AGRP-expressing neurons to the PVH neurons is important to increase appetite by favouring hyperphagia (Atasoy *et al*, 2012). Disrupting the composition of these ion channels could contribute to reduced PVH^{BDNF} neuronal firing, which awaits further investigations.

Female mice with a conditional knockout of *Rai1* from BDNF-producing neurons do not display a noteworthy difference in food intake. Conversely, their male counterparts exhibit a significant increase in food intake. Although SMS individuals of both genders tend to overeat, male patients who are obese show significantly higher food consumption than their female counterparts (Gandhi *et al.*, 2022). This observation raises the possibility that *Rai1* regulates eating behaviours through multiple cell types in the hypothalamus and that a male-specific involvement of BDNF-producing neurons in regulating food intake, potentially provides a neurobiological basis for the observed pattern in SMS patients (Gandhi et al., 2022). In future work, it would be interesting to dissect the sex-specific role of RAI1 in regulating the functional development of PVH^{BDNF} neurons. In addition to a role for RAI1 in regulating neuronal activity, RAI1 may regulate other aspects of PVH^{BDNF} neuronal function, including projections to other brain regions to regulate energy homeostasis. In this regard, it would be interesting to dissect how RAI1 controls the circuit connectivity of PVH^{BDNF} neurons and how *Rai1* loss in PVH^{BDNF} neurons affects nearby PVH^{TRKB} neurons that receive BDNF signalling and are linked to body weight regulation (An *et al.*, 2020).

At the molecular level, our RPPA data show that *Rai1* depletion disrupted multiple intracellular signalling pathways and resulted in the hypoactivation of specific phospho-signalling proteins.

Multiple early studies support the notion that Rai1 directly promotes *Bdnf* expression. First, hypothalamic *Bdnf* mRNA levels were reduced in SMS mice (Burns *et al.*, 2010; Javed *et al.*, 2021) or mice with *Rai1* conditional deletions (Huang *et al.*, 2016). Second, the RAI1 protein directly binds to a promoter region of *Bdnf* (Huang *et al.*, 2016). Finally, when *Rai1* expression was induced using CRISPR activation, *Bdnf* mRNA levels were significantly elevated (Chang *et al*, 2022a).

To lend further support, here we show that SMS mice have reduced hypothalamic BDNF protein levels, as well as reduced activation of a TRKB downstream target AKT. Reduced AKT activity is frequently associated with insulin resistance and obesity in mice (Shao *et al*, 2000) and children (Su *et al.*, 2021). We also found that obesity, increased HDL levels, and insulin insensitivity in SMS mice could be partially alleviated using a small molecule drug (LM22A-4) that promotes AKT phosphorylation. LM22A-4 penetrates the blood-brain barrier reasonably well and has been shown to ameliorate symptoms of other neurological disorders associated with BDNF dysfunction including Rett syndrome, Huntington's disease, Dravet syndrome, and refractory neonatal seizures (Canals *et al.*, 2004; Chang *et al.*, 2006; Gu *et al.*, 2022; Kron *et al.*, 2012; Ogier *et al.*, 2007). We recognize that while several in vivo studies have demonstrated the potential of LM22A-4 in targeting neurotrophin downstream signalling (Kron *et al*, 2014; Li *et al*, 2017), an in vitro analysis failed to demonstrate the ability of LM22A-4 to activate TRKB directly (Boltaev *et al*, 2017). Therefore, the precise mechanism by which LM22A-4 enhances AKT cascades in the mammalian brain remains unclear and awaits further investigations. In the hypothalamus of SMS mice, LM22A-4 could indirectly engage neurotrophin downstream PI3K-AKT pathway through the G protein-coupled receptor-dependent transactivation of the TRKB receptor (Domeniconi & Chao, 2010) or other unknown mechanisms. Moreover, while LM22A-

4 may have potential side effects, we found that wild-type mice treated with LM22A-4 did not show a further decrease in body weight, suggesting limited side effects regarding body weight regulation.

The partial rescue of SMS phenotypes that we observed contrasts with our previous findings that found (1) AAV-mediated BDNF overexpression in PVH at 3 weeks of age and (2) genetically overexpressing BDNF from early development could fully prevent the development of obesity in SMS mice (Javed *et al.*, 2021). Therefore, further increasing TRKB signalling activation and earlier intervention might improve therapeutic outcomes. Alternatively, our RPPA data showed that in addition to disruption of neurotrophin signalling, multiple pathways including mTOR were downregulated in SMS. Increasing hypothalamic mTOR activity has been shown to decrease food intake and body weight (Cota *et al.*, 2006). Therefore, it is possible that enhancing both mTOR and TRKB signalling could achieve a more robust rescue of obesity in SMS mice. Nevertheless, these data support the concept that drugging TRKB signalling may improve stereotypical repetitive behaviour and partially alleviate metabolic functions in a mouse model of SMS. Delayed symptom onset could provide a window of opportunity for other interventions to further modify disease progression, an area requiring further investigation.

This study has several limitations. First, whether the PVH^{BDNF} neurons depend on Rai1 to regulate adaptive thermogenesis awaits future analysis. It is known that a subset of posterior PVH^{BDNF} neurons project to the spinal cord and regulate thermogenesis (An *et al.*, 2015). However, we found the weights of brown adipocytes were similar in control and cKO mice. Moreover, SMS mice have normal respiratory exchange rates and there are currently no reports of defective adaptive thermogenesis in SMS patients. This suggests that adaptive thermogenesis is not impacted in SMS. Another limitation is that we did not test different doses, durations, and

time points for LM22A-4 treatment. The precise mechanisms by which LM22A-4 improves body weight, metabolic function, and repetitive behaviours remain unknown. Nevertheless, our work identifies RAI1 as a novel regulator of the neuronal excitability of PVH^{BDNF} neurons. This regulation is critical for regulating food intake and energy expenditure. Our evidence suggests that BDNF-producing neurons are involved in SMS pathogenesis and that enhancing BDNF-TRKB signalling should be explored as a future therapeutic avenue for obesity and metabolic conditions associated with reduced neurotrophin signalling (Xu & Xie, 2016).

Materials and Methods

Animal Management

The animal protocol (MUHC-8127) was approved by the animal care committee of the Montreal General Hospital and was performed according to the guidelines of the Canadian Council on Animal Care. Mice were group-housed in 12-hour light/12-hour dark cycles with an *ad libitum* supply of regular chow and water. The exception was in the fasting studies when the animals were food deprived for 5 hours and in CALMS and food intake studies when animals were single-housed in a 12-hour light/12-hour dark cycle with an *ad libitum* supply of regular chow and water. All mice were maintained in a C57Bl/6J background. *Bdnf*$^{Cre/Cre}$ (RRID: IMSR_JAX:030189), *Rosa26*$^{Ai9/Ai9}$ (RRID: IMSR_JAX:007909), and *Actb*$^{Cre/Cre}$ (RRID: IMSR_JAX:019099) mice were purchased from the Jackson laboratory. The *Rai1*$^{fl/fl}$ (RRID: IMSR_JAX:029103) strain was previously generated and characterized by us (Huang *et al.*, 2016). SMS mice (*Rai1*$^{+/-}$: whole-body germline *Rai1* heterozygous knockout that genetically mimics SMS) were generated by crossing germline *Actb*$^{Cre/Cre}$ mice with *Rai1*$^{fl/+}$. To generate conditional knockout mice, *Bdnf*$^{Cre/+}$; *Rai1*$^{fl/+}$ mice were crossed with *Rai1*$^{fl/+}$ to create control and experimental groups from the same littermate. 7 mice with malocclusion or lesions were excluded from the study: 4 with malocclusion (2 females and 2 males) and 3 with lesions (3 females).

Metabolic profiling

Metabolic profiling was conducted in three experimental conditions: male and female conditional knockout mice, female virus-injected *Bdnf*$^{Cre/+}$ mice, and female drug- or saline-injected SMS and control mice. Metabolic profiling included body weight and body composition

516 analysis, food intake measurement, indirect calorimetry for locomotion activity, energy
517 expenditure (EE), respiratory exchange rate (RER), measurement of serum lipids and leptin
518 levels, adipose tissue histology analysis, and glucose and insulin tolerance tests. All experiments
519 were performed as previously described (Javed *et al.*, 2021). A brief description is detailed
520 below.

521

522 *Body weight and body composition analysis*

523 The body weight of animals was measured weekly from week 3 (weaning age) onward. After the
524 25th week, mice were subjected to body composition analysis. Body composition, including total
525 fat and lean mass, was assessed using a nuclear EchoMRI whole-body analyzer. Toward the end
526 of the experiments, animals were euthanized to collect brown adipose, visceral, subcutaneous
527 (inguinal) and ependymal white adipose tissues and weighed using an analytical scale
528 (Sartorius).

529

530 *Food Intake Measurement*

531 Mice were single-housed for food intake measurement. Food intake was measured over a one-
532 week period during which food was weighed prior to placement in the cage with minimal
533 bedding. Each morning, the remaining food inside the cage was weighed. The amount of total
534 food consumed was averaged over 7 days.

535

536 *Indirect Calorimetry*

537 A Comprehensive Lab Animal Monitoring System (CLAM) (Columbus instruments) was used to
538 measure the RER and EE (normalized over lean mass). Animals were singled-housed in the
539 CLAMS apparatus at 21˚C (70˚F) in a light–dark cycle matching their housing conditions for 24
540 hours (acclimation), followed by 48 hours of measurement.

541

542 *Serum lipid level determination*

543 A fluorescence-based assay kit (Abcam ab65390) was used to measure serum lipid levels. The
544 manufacturer's instructions were followed except that we used half-area black 96-well
545 microplates. Fluorescence measurements at 535/587 nm (Ex/Em) were recorded with the Ensight
546 instrument from PerkinElmer. A new standard curve ranging from 0 to 10 μg/ml was produced
547 for each microplate to accurately determine lipid levels in serum samples. Standards and samples
548 were loaded and analyzed twice.

549

550 *Histology of adipose tissue*

551 Ependymal white adipose tissues (WAT) were excised immediately after the animals were
552 euthanized and fixed with 10% formalin in PBS. The fixed tissues were dehydrated, embedded in
553 paraffin, and sectioned. Two 5-micrometre thick sections were taken from each animal and
554 stained with hematoxylin and eosin. Images of sections were then captured using an Aperio
555 ScanScope CS slide scanner at 20X optical magnification, and the resulting images were saved
556 in jpeg format using the ImageScope software. The images were manually cleaned to remove
557 non-adipose tissues such as lymph nodes. An automated method using the Adiposoft plugin
558 version 1.16 was utilized to determine adipocyte size and number from the jpeg images in Fiji

559 version 2.1.0/1.53c. The Adiposoft settings used excluded cells on edges and set a minimum and
560 maximum cell diameter of 20 and 300 µm, respectively. An experimental value of 2.49 µm per
561 pixel was determined using the Aperio scale bar and used for Adiposoft. To ensure accuracy, two
562 images from each animal were analyzed blindly, examining more than 1600 cells per mouse and
563 more than 9100 cells per condition. Adipocyte size frequencies were calculated using the
564 frequency function in Excel.

565

566 *Glucose and insulin tolerance tests*

567 For the glucose tolerance test, experimental mice were food deprived for 5 hours with *ad libitum*
568 water supply. A bolus of glucose (1.5g/kg of lean body weight) was then administered
569 intraperitoneally and glycemia was measured from tail vein blood samples using the Accu-chek
570 Performa glucometer at T0 (before the injection) as well as at 15, 30, 45, 60, 90 and 120 min
571 (after the injection). Tail vein blood samples were collected via a capillary for insulin assays at
572 T0, 15 and 30 min. For insulin tolerance tests, experimental mice were food-deprived for 5 hours
573 with *ad libitum* access to water. A bolus of insulin (1 U/kg of lean body weight) was
574 administered via an IP injection and glycemia was measured from blood sampled at the tail vein
575 using an Accu-chek Performa glucometer at T0 (before the injection), as well as at 15, 30, 45, 60,
576 90 and 120 min (after the injection). Tail vein blood samples were collected via a capillary for
577 insulin assays at T0.

578

579 **Stereotaxic Injections**

580 *Bdnf*$^{Cre/+}$ mice were anesthetized using isoflurane, and the ears were barred onto a stereotaxic
581 device (David Kopf Instruments). Adeno-associated viruses (AAVs, volume = 250 nl) were
582 bilaterally injected into the PVH using the following coordinates relative to the Bregma: -0.6 mm
583 anteroposterior (AP), ±0.35 mm mediolateral (ML) and -5.52 mm dorsoventral (DV). A
584 description of the AAV constructs and titre used is detailed below:

585 AAV9-CMV7-DIO-saCas9 (Viral title: >1 × 10^13), Vector Biolab

586 AAV9-CMV7-sgRai1-GFP (Viral title: >1 ×10^9), Applied Biological Materials Inc. Three
587 sgRNAs were pooled to target Rai1 (sgRNA1: TTCCTCGCCAGAGTAGCGCC, sgRNA2:
588 CCCAGCCTCATGATAGGCCG, sgRNA3: CCCAGCCTCATGATAGGCCG).

589

590 **Immunostaining of mouse brain tissues**

591 Immunostaining experiments were performed as previously described (Huang *et al*, 2012).
592 Briefly, mice were anesthetized and perfused with 1X PBS and 4% formaldehyde, and the brains
593 were dissected and fixed in 4% formaldehyde overnight. Fixed brains were transferred to 30%
594 sucrose solution and subsequently embedded in the OCT solution. The brains were then
595 sectioned (40µm), washed in PBS, permeabilized with 0.5% Triton X-100, and incubated with
596 10% normal donkey serum in PBS for 2 hours. The sections were then incubated overnight with
597 primary antibodies (Rai1: 1:500 dilution, RRID:AB_2921229 (Huang *et al.*, 2016); BDNF:
598 1:500, RRID:AB_10862052, Abcam ab108319; p-TRKB: 1:500 dilution, RRID:AB_2721199,
599 Millipore ABN1381; oxytocin: 1:1000 dilution, RRID:AB_11212999, Millipore MAB5296) at
600 4°C on a shaker. The following day, sections were washed with 1X PBS twice for 10 minutes
601 and incubated with a secondary antibody (1:1000 dilution) for 3 hours at room temperature.

602 Sections were washed with 1X PBS once before mounting on glass slides with the DAPI-
603 mounting (DAPI-Fluoromount-G, SouthernBiotech) and then imaged using a confocal
604 microscope (Olympus FV-1000 confocal laser scanning microscope) with 20x or 40x objectives
605 (NA 0.85 and 1.3, respectively). Z-stacks were taken with a step size of 1.0 μm with a 1024 x
606 1024 resolution. Images were acquired as a stack with at least 13 optical sections. Image analysis
607 was performed using the Fiji software.

608

609 **Real-Time Quantitative Reverse Transcription PCR (qRT-PCR)**

610 qRT-PCR was performed using mRNAs isolated from hypothalamic tissue samples. After the
611 isolation of total RNA, mRNAs were reverse-transcribed with the SuperScript III First-Strand
612 Synthesis System (Thermo-Fisher). Quantitative PCR reactions were conducted using SsoFast
613 EvaGreen Supermix on a Bio-Rad qPCR system.

614

615 **Enzyme-linked immunosorbent assay (ELISA)**

616 ELISA was performed using hypothalamic tissues from 7-week-old SMS mice to assess the
617 mature BDNF protein levels using a commercially available BDNF ELISA kit (Mature BDNF
618 Rapid ELISA Kit: Human, Mouse, Rat).

619

620 **Western blotting analysis**

621 Mice were quickly decapitated, brains were rapidly removed, and hypothalamic tissues were
622 collected, weighed, and snap-frozen with liquid nitrogen. Hypothalamic tissues were lysed using

623 a tissue lysis buffer containing RIPA buffer (5M NaCl, 1M PH 8.0 Tris HCl, 1% NP.40, 10%
624 $C_{24}H_{39}NaO_4$, and 20% SDS) and the Halt™ Protease and Phosphatase Inhibitor Cocktail
625 (Thermo-Fisher). Lysates were first sonicated on ice for 15 seconds and centrifuged at 10000
626 RPM at 4°C for 10 minutes. The supernatant was collected in a separate Eppendorf tube, and a
627 BCA assay was performed to quantify protein levels. Proteins were then separated using SDS-
628 PAGE gel and transferred onto nitrocellulose membranes. To determine the phosphorylation
629 levels of AKT, membranes were cut and blocked in 5% milk in tris-buffered saline (TBS) for 1
630 hour and then incubated overnight at 4°C with anti-p-AKT (Ser473) antibody (1:1000 dilution,
631 RRID: AB_2315049, Cell Signaling Technology 4060T) and anti-H3 antibody (internal control:
632 1:1000 dilution, RRID: AB_302613, Abcam ab1791). The next day, membranes were washed
633 with TBST three times for five minutes before incubating with an HRP-conjugated secondary
634 antibody (1:10000 dilution, Thermo Fisher 200-403-095S). Membranes were later stripped by
635 incubating in 0.5M NaOH for 10 min and then re-probed for total Akt levels by incubating with
636 anti-Akt (C67E7) antibody (1:1000 dilution, Cell Signaling Technology 4691T). The density of
637 each immunoreactive phospho-protein band was expressed as a fraction of the band for the total
638 AKT protein in the same lane.

639

640 **Reverse-phase protein array (RPPA)**

641 A reverse-phase protein array (RPPA) was used for precise high-throughput quantification of
642 total and phospho-protein levels in different signalling pathways. Protein lysates from
643 hypothalamic tissues were extracted and transferred to 384-well microarray plates to print
644 individual slides. The slides were then labelled with validated antibodies recognizing total
645 protein and specific phosphorylation sites. SYPRO Ruby staining was used to measure total

646 protein levels. The data obtained from RPPA were normalized for individual samples. Each
647 antibody's raw signal intensity (SI) was determined by subtracting the background from the
648 antibody-specific signals during image analysis. The normalized antibody SI was expressed
649 using the formula N = A - C/T x M, where N is the normalized SI, A is the raw antibody SI, C is
650 the negative control SI, T is the SI of total protein, and M is the median SI of total protein from a
651 spot within the same sample group. Antibodies with SI less than 200 were filtered out, and
652 quality control (QC) scores were established to discard poor-quality reactions. The coefficient of
653 variation (CV) score was determined for each antibody and defined as the percentage of samples
654 on a slide with a CV < 20%. Antibodies with a median technical triplicate CV >20% were also
655 excluded from further analysis. T-tests were performed for each antibody to identify
656 differentially expressed proteins in the SMS compared to control groups. PCA plots were
657 generated for all samples, annotated with their experimental group, and hierarchical clustering
658 was performed using a Python analysis tool. The vertical axis of the dendrogram represents the
659 dissimilarity (measured as distance) between protein expressions, and the horizontal axis
660 represents the individual test samples. The colour code (ranging from red to yellow to green)
661 specifies the expression levels of different proteins, where red indicates low expression, yellow
662 indicates intermediate expression, and green indicates high expression. Enrichment analysis on
663 the differentially expressed proteins was performed using an online data resource string: version
664 11.5.

665

666 **Electrophysiology of acute brain slices**

667 Mouse brains were removed and placed in ice-cold carbonated slicing artificial cerebrospinal
668 fluid (aCSF), which contained (in mM) 124 NaCl, 3 KCl, 1.4 NaH_2PO_4, 26 $NaHCO_3$,1.3 Mg

669 SO4, 10 D-glucose, 0.5 $CaCl_2$, and 3.5 $MgCl_2$. Coronal sections (300 µm) were cut on a
670 vibratome. Slices were allowed to recover at 32 °C for 40 minutes and then at 30 °C for
671 30 minutes to 6 hours in the recording medium, carbonated aCSF (124 NaCl, 3 KCl, 1.4
672 NaH_2PO_4, 26 $NaHCO_3$,1.3 Mg SO4, 10 D-glucose, 2.4 $CaCl_2$, in mM, ~300 mOsm). Signals
673 were recorded with a 5× gain, low-pass filtered at 2 kHz, digitized at 10 kHz (Molecular
674 Devices Multiclamp 700B) and analyzed with pClamp 11 (Molecular Devices). Whole-cell
675 recordings were made using 3–5 MΩ pipettes filled with an internal solution that contained
676 (in mM) 131 potassium gluconate, 8 NaCl, 20 KCl, 2 EGTA, 10 HEPES, 2 MgATP and 0.3
677 Na3GTP (pH 7.2, with KOH, 300–310 mOsm with sucrose). For miniature current recording,
678 the internal solution contained (in mM) 130 gluconate acid, 8 CsCl, 1 NaCl, 2 EGTA, 0.8
679 CsOH, 10 HEPES, 2 MgATP and 0.3 Na3GTP (pH 7.2, with CsOH, 300–310 mOsm adjusted
680 with sucrose). mEPSCs were recorded in the presence of 1 µM TTX at a holding potential of -
681 70 mV. mIPSCs were recorded at a holding potential of +10 mV. The mIPSCs were analyzed
682 from events during a 2-minute continuous recording that contained > 15 events/neuron.
683 Additional calculations, statistical analysis, and plotting were performed in Microsoft Excel or
684 Prism (GraphPad).

685

686 **Spectrometric analysis of LM22A-4 levels in the brain**

687 We assessed the efficacy of LM22A-4, a small molecule pharmacological agent, in 8-week-old
688 SMS and control mice. LM22A-4, chemical name N1, N3, N5tris (2hydroxyethyl) 1, 3, 5
689 benzenetricarboxamide (Molecular formula: $C_{15}H_{21}N_3O_6$, Formula weight: 339.3), was
690 manufactured by Cayman Chemical with purity specification >98%. A stock solution was made
691 by first dissolving LM22A-4 in DMSO (solubility =30mg/ml) and then diluting it with 0.9%

692 isotonic sterilized saline solution (Sigma). To maximize brain concentrations, LM22A-4 was
693 administered both intranasally (5mg/kg) and intraperitoneally (50mg/kg), as previously reported
694 (Simmons *et al*, 2013). The bioavailability of this drug in the hypothalamus using these doses
695 and routes of administration was assessed with the reverse phase LC triple-quadrupole tandem
696 mass spectroscopic detection (LC-MS/MS) by Absorption Systems. Mice were euthanized, and
697 hypothalamic tissue was collected at either 1 h or 3 h post-injection (n= 4/timepoint). Known
698 amounts of LM22A-4 were added to the blank sample to generate a standard curve to verify test
699 accuracy.

700

701 **LM22A-4 treatment**

702 Mice were divided into four groups: Saline-injected control, Saline-injected SMS, LM22A-4-
703 injected SMS, and LM22A-4-injected control mice. Mice were injected daily, intra-nasally
704 (5mg/kg) and intraperitoneally (50mg/kg), for 7 weeks. Body weight was measured between 8
705 and 14 weeks of age. Food intake was measured from 14 to 15 weeks of age. After 15 weeks of
706 age, mice were euthanized to collect brown adipose, visceral, subcutaneous (inguinal) and
707 ependymal white adipose tissues and weighed using an analytical scale (Sartorius).
708 Hypothalamic brain tissues were collected for western blot analysis. Metabolic profiling was
709 performed on a separate cohort of mice injected for two weeks prior to the start of experiments
710 as well as at specific weeks during the experiment.

711

712 **Vertical rearing**

To measure vertical repetitive rearing, mice were taken into the testing room and allowed to habituate for 1 h prior to testing. During the test, mice were placed in the center of a 45 cm (W) × 45 cm (D) × 40 cm (H) square arena, and their movement was recorded for 10 minutes.

Statistical analysis

The sample sizes used were based on our previous studies (Huang *et al.*, 2016; Javed *et al.*, 2021). The data were subjected to statistical analysis for significance by using GraphPad Prism 0.9. Significance was defined as having a p-value < 0.05. The significance levels were as follows: * p< 0.05, **p<0.01, ***p<0.0001, **** p<0.0001. The statistical tests used for each analysis (e.g., Student's t-test, analysis of variance [ANOVA]) are indicated in the text and legends.

Data Availability

This study includes no data deposited in external repositories.

Acknowledgements

Sehrish Javed was supported by a Fonds de Recherche du Québec - Santé (FRQS) doctoral award. This work was supported by the Rare Diseases: Models & Mechanisms Network and the Smith-Magenis syndrome Research Foundation.

References

Abad C, Cook MM, Cao L, Jones JR, Rao NR, Dukes-Rimsky L, Pauly R, Skinner C, Wang Y, Luo F *et al* (2018) A Rare De Novo RAI1 Gene Mutation Affecting BDNF-Enhancer-Driven Transcription Activity Associated with Autism and Atypical Smith-Magenis Syndrome Presentation. *Biology (Basel)* 7

Alaimo JT, Barton LV, Mullegama SV, Wills RD, Foster RH, Elsea SH (2015) Individuals with Smith-Magenis syndrome display profound neurodevelopmental behavioral deficiencies and exhibit food-related behaviors equivalent to Prader-Willi syndrome. *Res Dev Disabil* 47: 27-38

An JJ, Kinney CE, Tan JW, Liao GY, Kremer EJ, Xu B (2020) TrkB-expressing paraventricular hypothalamic neurons suppress appetite through multiple neurocircuits. *Nat Commun* 11: 1729

An JJ, Liao GY, Kinney CE, Sahibzada N, Xu B (2015) Discrete BDNF Neurons in the Paraventricular Hypothalamus Control Feeding and Energy Expenditure. *Cell Metab* 22: 175-188

Atasoy D, Betley JN, Su HH, Sternson SM (2012) Deconstruction of a neural circuit for hunger. *Nature* 488: 172-177

Balthasar N, Dalgaard LT, Lee CE, Yu J, Funahashi H, Williams T, Ferreira M, Tang V, McGovern RA, Kenny CD *et al* (2005) Divergence of melanocortin pathways in the control of food intake and energy expenditure. *Cell* 123: 493-505

Boltaev U, Meyer Y, Tolibzoda F, Jacques T, Gassaway M, Xu Q, Wagner F, Zhang YL, Palmer M, Holson E *et al* (2017) Multiplex quantitative assays indicate a need for reevaluating reported small-molecule TrkB agonists. *Sci Signal* 10

Boot E, Linders CC, Tromp SH, van den Boogaard MJ, van Eeghen AM (2021) Possible underreporting of pathogenic variants in RAI1 causing Smith-Magenis syndrome. *Am J Med Genet A* 185: 3167-3169

Burke LK, Darwish T, Cavanaugh AR, Virtue S, Roth E, Morro J, Liu SM, Xia J, Dalley JW, Burling K *et al* (2017) mTORC1 in AGRP neurons integrates exteroceptive and interoceptive food-related cues in the modulation of adaptive energy expenditure in mice. *Elife* 6

Burns B, Schmidt K, Williams SR, Kim S, Girirajan S, Elsea SH (2010) Rai1 haploinsufficiency causes reduced Bdnf expression resulting in hyperphagia, obesity and altered fat distribution in mice and humans with no evidence of metabolic syndrome. *Hum Mol Genet* 19: 4026-4042

Canals JM, Checa N, Marco S, Akerud P, Michels A, Perez-Navarro E, Tolosa E, Arenas E, Alberch J (2001) Expression of brain-derived neurotrophic factor in cortical neurons is regulated by striatal target area. *J Neurosci* 21: 117-124

Canals JM, Pineda JR, Torres-Peraza JF, Bosch M, Martin-Ibanez R, Munoz MT, Mengod G, Ernfors P, Alberch J (2004) Brain-derived neurotrophic factor regulates the onset and severity of motor dysfunction associated with enkephalinergic neuronal degeneration in Huntington's disease. *J Neurosci* 24: 7727-7739

Caron A, Labbe SM, Lanfray D, Blanchard PG, Villot R, Roy C, Sabatini DM, Richard D, Laplante M (2016) Mediobasal hypothalamic overexpression of DEPTOR protects against high-fat diet-induced obesity. *Mol Metab* 5: 102-112

Chang HC, Lee YJ, Javed S, Haque M, Chang YT, Lin YC, Oram C, Huang WH (2022a) rAAV-CRISPRa therapy corrects Rai1 haploinsufficiency and rescues selective disease features in Smith-Magenis syndrome mice. *J Biol Chem*: 102728

Chang Q, Khare G, Dani V, Nelson S, Jaenisch R (2006) The disease progression of Mecp2 mutant mice is affected by the level of BDNF expression. *Neuron* 49: 341-348

Chang YT, Kowalczyk M, Fogerson PM, Lee YJ, Haque M, Adams EL, Wang DC, DeNardo LA, Tessier-Lavigne M, Huguenard JR *et al* (2022b) Loss of Rai1 enhances hippocampal excitability and epileptogenesis in mouse models of Smith-Magenis syndrome. *Proc Natl Acad Sci U S A* 119: e2210122119

Collaboration NCDRF (2017) Worldwide trends in body-mass index, underweight, overweight, and obesity from 1975 to 2016: a pooled analysis of 2416 population-based measurement studies in 128.9 million children, adolescents, and adults. *Lancet* 390: 2627-2642

Colmers PLW, Bains JS (2018) Balancing tonic and phasic inhibition in hypothalamic corticotropin-releasing hormone neurons. *J Physiol* 596: 1919-1929

Cota D, Proulx K, Smith KA, Kozma SC, Thomas G, Woods SC, Seeley RJ (2006) Hypothalamic mTOR signaling regulates food intake. *Science* 312: 927-930

Domeniconi M, Chao MV (2010) Transactivation of Trk receptors in spinal motor neurons. *Histol Histopathol* 25: 1207-1213

Edelman EA, Girirajan S, Finucane B, Patel PI, Lupski JR, Smith AC, Elsea SH (2007) Gender, genotype, and phenotype differences in Smith-Magenis syndrome: a meta-analysis of 105 cases. *Clin Genet* 71: 540-550

Gandhi AA, Wilson TA, Sisley S, Elsea SH, Foster RH (2022) Relationships between food-related behaviors, obesity, and medication use in individuals with Smith-Magenis syndrome. *Res Dev Disabil* 127: 104257

Gao H, Molinas AJR, Miyata K, Qiao X, Zsombok A (2017) Overactivity of Liver-Related Neurons in the Paraventricular Nucleus of the Hypothalamus: Electrophysiological Findings in db/db Mice. *J Neurosci* 37: 11140-11150

Garcia AD, Doan NB, Imura T, Bush TG, Sofroniew MV (2004) GFAP-expressing progenitors are the principal source of constitutive neurogenesis in adult mouse forebrain. *Nat Neurosci* 7: 1233-1241

Gorski JA, Talley T, Qiu M, Puelles L, Rubenstein JL, Jones KR (2002) Cortical excitatory neurons and glia, but not GABAergic neurons, are produced in the Emx1-expressing lineage. *J Neurosci* 22: 6309-6314

Gray J, Yeo GS, Cox JJ, Morton J, Adlam AL, Keogh JM, Yanovski JA, El Gharbawy A, Han JC, Tung YC *et al* (2006) Hyperphagia, severe obesity, impaired cognitive function, and hyperactivity associated with functional loss of one copy of the brain-derived neurotrophic factor (BDNF) gene. *Diabetes* 55: 3366-3371

Gu F, Parada I, Yang T, Longo FM, Prince DA (2022) Chronic partial TrkB activation reduces seizures and mortality in a mouse model of Dravet syndrome. *Proc Natl Acad Sci U S A* 119

Huang WH, Guenthner CJ, Xu J, Nguyen T, Schwarz LA, Wilkinson AW, Gozani O, Chang HY, Shamloo M, Luo L (2016) Molecular and Neural Functions of Rai1, the Causal Gene for Smith-Magenis Syndrome. *Neuron* 92: 392-406

Huang WH, Tupal S, Huang TW, Ward CS, Neul JL, Klisch TJ, Gray PA, Zoghbi HY (2012) Atoh1 governs the migration of postmitotic neurons that shape respiratory effectiveness at birth and chemoresponsiveness in adulthood. *Neuron* 75: 799-809

Huang WH, Wang DC, Allen WE, Klope M, Hu H, Shamloo M, Luo L (2018) Early adolescent Rai1 reactivation reverses transcriptional and social interaction deficits in a mouse model of Smith-Magenis syndrome. *Proc Natl Acad Sci U S A*

Javed S, Lee YJ, Xu J, Huang WH (2021) Temporal dissection of Rai1 function reveals brain-derived neurotrophic factor as a potential therapeutic target for Smith-Magenis syndrome. *Hum Mol Genet* 31: 275-288

Javed S, Selliah T, Lee YJ, Huang WH (2020) Dosage-sensitive genes in autism spectrum disorders: From neurobiology to therapy. *Neurosci Biobehav Rev* 118: 538-567

Kamitakahara A, Xu B, Simerly R (2016) Ventromedial hypothalamic expression of Bdnf is required to establish normal patterns of afferent GABAergic connectivity and responses to hypoglycemia. *Mol Metab* 5: 91-101

Kocalis HE, Hagan SL, George L, Turney MK, Siuta MA, Laryea GN, Morris LC, Muglia LJ, Printz RL, Stanwood GD *et al* (2014) Rictor/mTORC2 facilitates central regulation of energy and glucose homeostasis. *Mol Metab* 3: 394-407

825 Kron M, Howell CJ, Adams IT, Ransbottom M, Christian D, Ogier M, Katz DM (2012) Brain activity
826 mapping in Mecp2 mutant mice reveals functional deficits in forebrain circuits, including key nodes in
827 the default mode network, that are reversed with ketamine treatment. *J Neurosci* 32: 13860-13872
828 Kron M, Lang M, Adams IT, Sceniak M, Longo F, Katz DM (2014) A BDNF loop-domain mimetic acutely
829 reverses spontaneous apneas and respiratory abnormalities during behavioral arousal in a mouse model
830 of Rett syndrome. *Dis Model Mech* 7: 1047-1055
831 Lee SK, Lee S, Shin SY, Ryu PD, Lee SY (2012) Single cell analysis of voltage-gated potassium channels that
832 determines neuronal types of rat hypothalamic paraventricular nucleus neurons. *Neuroscience* 205: 49-
833 62
834 Li W, Bellot-Saez A, Phillips ML, Yang T, Longo FM, Pozzo-Miller L (2017) A small-molecule TrkB ligand
835 restores hippocampal synaptic plasticity and object location memory in Rett syndrome mice. *Dis Model*
836 *Mech* 10: 837-845
837 Loos RJF, Yeo GSH (2022) The genetics of obesity: from discovery to biology. *Nat Rev Genet* 23: 120-133
838 Massa SM, Yang T, Xie Y, Shi J, Bilgen M, Joyce JN, Nehama D, Rajadas J, Longo FM (2010) Small molecule
839 BDNF mimetics activate TrkB signaling and prevent neuronal degeneration in rodents. *J Clin Invest* 120:
840 1774-1785
841 Miki T, Liss B, Minami K, Shiuchi T, Saraya A, Kashima Y, Horiuchi M, Ashcroft F, Minokoshi Y, Roeper J *et al*
842 (2001) ATP-sensitive K+ channels in the hypothalamus are essential for the maintenance of glucose
843 homeostasis. *Nat Neurosci* 4: 507-512
844 Moss J, Oliver C, Arron K, Burbidge C, Berg K (2009) The prevalence and phenomenology of repetitive
845 behavior in genetic syndromes. *J Autism Dev Disord* 39: 572-588
846 Ogier M, Wang H, Hong E, Wang Q, Greenberg ME, Katz DM (2007) Brain-derived neurotrophic factor
847 expression and respiratory function improve after ampakine treatment in a mouse model of Rett
848 syndrome. *J Neurosci* 27: 10912-10917
849 Parton LE, Ye CP, Coppari R, Enriori PJ, Choi B, Zhang CY, Xu C, Vianna CR, Balthasar N, Lee CE *et al* (2007)
850 Glucose sensing by POMC neurons regulates glucose homeostasis and is impaired in obesity. *Nature* 449:
851 228-232
852 Perry CA, Pravetoni M, Teske JA, Aguado C, Erickson DJ, Medrano JF, Lujan R, Kotz CM, Wickman K (2008)
853 Predisposition to late-onset obesity in GIRK4 knockout mice. *Proc Natl Acad Sci U S A* 105: 8148-8153
854 Quarta C, Claret M, Zeltser LM, Williams KW, Yeo GSH, Tschop MH, Diano S, Bruning JC, Cota D (2021)
855 POMC neuronal heterogeneity in energy balance and beyond: an integrated view. *Nat Metab* 3: 299-308
856 Rao NR, Abad C, Perez IC, Srivastava AK, Young JI, Walz K (2017) Rai1 Haploinsufficiency Is Associated
857 with Social Abnormalities in Mice. *Biology (Basel)* 6
858 Schultze SM, Hemmings BA, Niessen M, Tschopp O (2012) PI3K/AKT, MAPK and AMPK signalling: protein
859 kinases in glucose homeostasis. *Expert Rev Mol Med* 14: e1
860 Shao J, Yamashita H, Qiao L, Friedman JE (2000) Decreased Akt kinase activity and insulin resistance in
861 C57BL/KsJ-Leprdb/db mice. *J Endocrinol* 167: 107-115
862 Simmons DA, Belichenko NP, Yang T, Condon C, Monbureau M, Shamloo M, Jing D, Massa SM, Longo FM
863 (2013) A small molecule TrkB ligand reduces motor impairment and neuropathology in R6/2 and BACHD
864 mouse models of Huntington's disease. *J Neurosci* 33: 18712-18727
865 Slager RE, Newton TL, Vlangos CN, Finucane B, Elsea SH (2003) Mutations in RAI1 associated with Smith-
866 Magenis syndrome. *Nat Genet* 33: 466-468
867 Smith AC, Magenis RE, Elsea SH (2005) Overview of Smith-Magenis syndrome. *J Assoc Genet Technol* 31:
868 163-167
869 Smith AC, McGavran L, Robinson J, Waldstein G, Macfarlane J, Zonona J, Reiss J, Lahr M, Allen L, Magenis
870 E (1986) Interstitial deletion of (17)(p11.2p11.2) in nine patients. *Am J Med Genet* 24: 393-414

871 Smith MA, Katsouri L, Irvine EE, Hankir MK, Pedroni SM, Voshol PJ, Gordon MW, Choudhury AI, Woods A,
872 Vidal-Puig A *et al* (2015) Ribosomal S6K1 in POMC and AgRP Neurons Regulates Glucose Homeostasis
873 but Not Feeding Behavior in Mice. *Cell Rep* 11: 335-343
874 Su X, Gu D, Xu L, Liang Z, Luo X, Yang P, Yang J (2021) PI3K/Akt pathway expression in children with
875 different obesity degrees and its relationship with glucolipid metabolism and insulin resistance. *Am J*
876 *Transl Res* 13: 6592-6598
877 Tan CL, Cooke EK, Leib DE, Lin YC, Daly GE, Zimmerman CA, Knight ZA (2016) Warm-Sensitive Neurons
878 that Control Body Temperature. *Cell* 167: 47-59 e15
879 Taniguchi H, He M, Wu P, Kim S, Paik R, Sugino K, Kvitsiani D, Kvitsani D, Fu Y, Lu J *et al* (2011) A resource
880 of Cre driver lines for genetic targeting of GABAergic neurons in cerebral cortex. *Neuron* 71: 995-1013
881 Unger TJ, Calderon GA, Bradley LC, Sena-Esteves M, Rios M (2007) Selective deletion of Bdnf in the
882 ventromedial and dorsomedial hypothalamus of adult mice results in hyperphagic behavior and obesity.
883 *J Neurosci* 27: 14265-14274
884 Vohra MS, Benchoula K, Serpell CJ, Hwa WE (2022) AgRP/NPY and POMC neurons in the arcuate nucleus
885 and their potential role in treatment of obesity. *Eur J Pharmacol* 915: 174611
886 Wu SW, Xu B (2022) Rapid and Lasting Effects of Activating BDNF-Expressing PVH Neurons on Energy
887 Balance. *eNeuro* 9
888 Xu B, Goulding EH, Zang K, Cepoi D, Cone RD, Jones KR, Tecott LH, Reichardt LF (2003) Brain-derived
889 neurotrophic factor regulates energy balance downstream of melanocortin-4 receptor. *Nat Neurosci* 6:
890 736-742
891 Xu B, Xie X (2016) Neurotrophic factor control of satiety and body weight. *Nat Rev Neurosci* 17: 282-292
892 Xu Y, Lu Y, Cassidy RM, Mangieri LR, Zhu C, Huang X, Jiang Z, Justice NJ, Xu Y, Arenkiel BR *et al* (2019)
893 Identification of a neurocircuit underlying regulation of feeding by stress-related emotional responses.
894 *Nat Commun* 10: 3446
895 Yang H, An JJ, Sun C, Xu B (2016) Regulation of Energy Balance via BDNF Expressed in Nonparaventricular
896 Hypothalamic Neurons. *Mol Endocrinol* 30: 494-503
897 Yeo GS, Connie Hung CC, Rochford J, Keogh J, Gray J, Sivaramakrishnan S, O'Rahilly S, Farooqi IS (2004) A
898 de novo mutation affecting human TrkB associated with severe obesity and developmental delay. *Nat*
899 *Neurosci* 7: 1187-1189

900

901

902

903 **Figures and Figure legends**

904 **Figure 1: *Rai1* haploinsufficiency disrupts hypothalamic proteomic profile in mice**

905 **(A)** ELISA showing that BDNF protein levels in hypothalamic tissues were significantly reduced
906 in SMS mice compared to controls (n=4/genotype). *p<0.05, unpaired t-test, two-tailed.

907 **(B)** A schematic diagram showing the experimental strategy. Hypothalamic tissue lysates from 7-
908 week-old control (n = 5, technical triplicates/sample) and SMS (n=8, technical
909 triplicates/sample) mice were subjected to RPPA that utilizes a cocktail of 240 validated
910 antibodies to probe several key intracellular signalling pathways by quantifying the expression
911 levels of total and phosphorylated proteins

912 **(C)** Principal component analysis segregates the SMS and Ctrl groups where PC1 explains 47%
913 of the variance, and PC2 explains 25% of the variance.

914 **(D)** Heat map showing hierarchical clustering of differentially expressed phospho-proteins: most
915 showed reduced levels in SMS samples.

916 **(E)** Protein-protein interaction (PPI) analysis showing differentially expressed proteins and
917 phospho-proteins in a crosstalk network. PPI enrichment p-value: < 1.0e-16. The nodes represent
918 the proteins/phospho-proteins and the lines indicate physical interactions. Associations with
919 specific molecular pathways are shown as color-coded outer rings.

920 **(F-G)** The protein levels of two neurotrophin pathway-related nodes, PIK3CA (**F**) and phospho-
921 NF-kB (**G**), were significantly reduced in SMS samples. ****p<0.0001, unpaired t-test, two-
922 tailed

923

924 **Figure 2: RAI1 is required in BDNF-producing cells to regulate energy metabolism**

925 **(A)** A schematic diagram showing selective deletion of *Rai1* from BDNF-producing cells in
926 mice.

927 **(B)** Representative images showing that in Ctrl mice (*Bdnf*$^{Cre/+}$; *Ai9*), many PVH^{BDNF} neurons
928 (magenta) express RAI1 (cyan, double-positive cells were indicated with yellow arrows). By

929 contrast, PVH^{BDNF} neurons lack RAI1 expression in the cKO group (*Bdnf*$^{Cre/+}$; *Rai1*$^{fl/fl}$; *Ai9*).
930 Scale bars = 20μm.

931 **(C)** Percentage of PVH^{BDNF} neurons co-expressing RAI1 in Ctrl (n=3) and cKO (n=3) mice.
932 unpaired t-test, two-tailed, ****p<0.0001.

933 **(D)** Female cKO mice (n = 12) showed a significant weight gain when compared to female Ctrl
934 mice (n = 10). Two-way ANOVA with Šidák's multiple comparisons test. *p<0.05, ***p<0.001.

935 **(E)** Body composition was measured with Echo-MRI, showing an increased fat mass in 26-
936 week-old mice. ns indicates the difference is not significant. Two-way ANOVA with Šidák's
937 multiple comparisons test. ****p<0.0001.

938 **(F)** Fat mass of brown adipocytes (BAT), subcutaneous inguinal (S.C.ing) and epididymal white
939 adipose tissue (eWAT) in Ctrl and cKO mice. ns indicates the difference is not significant. Two-
940 way ANOVA with Šidák's multiple comparisons test. **p<0.01, ****p<0.0001.

941 **(G)** Representative images showing eWAT adipocyte hypertrophy of the cKO mice (left). Scale
942 bar = 500μm. Frequency distribution of adipocytes at each cellular size (right). Two-way
943 ANOVA with Šidák's multiple comparisons test. ***p<0.001, ****p<0.0001.

944 **(H)** Female cKO mice showed significantly increased blood leptin levels. unpaired t-test, two-
945 tailed, **p<0.01.

946 **(I)** Female cKO mice showed reduced energy expenditure during the dark phase. ns indicates not
947 significantly different. Two-way ANOVA with Šidák's multiple comparisons test. *p<0.05.

948 **(J)** Female cKO mice showed reduced locomotor activity during the dark phase. ns indicates the
949 difference is not significant. Two-way ANOVA with Šidák's multiple comparisons test. *p<0.05.

950 **(K)** Female cKO mice showed similar food intake as control mice. ns indicates not significant.
951 unpaired t-test, two-tailed.

952 **(L)** Glucose tolerance test showing that female cKO mice became hyperglycemic 20 minutes
953 after intraperitoneal glucose administration, suggesting glucose intolerance. Two-way ANOVA
954 with Šidák's multiple comparisons test. *p<0.05, ***p<0.001.

955 Data are shown as mean±SEM.

956

957

958 **Figure 3: *Rai1* loss reduces intrinsic neuronal excitability and enhances inhibitory synaptic**
959 **transmission of PVH^{BDNF} neurons**

960 **(A)** A representative image showing a patched PVH^{BDNF} neuron labelled by *Bdnf*^{Cre}-dependent
961 tdTomato fluorescence signals.

962 **(B-C)** Representative traces of spontaneous firing of control (black) and cKO (red) neurons at a
963 holding voltage of -60mV **(B)**. The average spontaneous AP firing frequencies are shown in **(C)**.
964 *p<0.05, unpaired student's t-tests.

965 **(D)** The resting membrane potentials of control (black) and cKO (red) PVH^{BDNF} neurons.
966 **p<0.01, unpaired student's t-tests.

967 **(E-F)** The number of control (black) and cKO (red) PVH^{BDNF} neurons that showed spontaneous
968 firing (open) or are silent (solid) at resting membrane potentials **(E)** and a holding voltage of -
969 70mV **(F)**.

970 **(G)** Representative traces of elicited APs in control (black) and cKO (red) PVH^{BDNF} neurons
971 responding to an inject current (bottom, blue), which ramps up from the resting membrane
972 potentials at 1 nA per second for 500ms.

973 **(H)** The threshold of the first AP initiated by a current ramp in control (black) and cKO (red)
974 PVH^{BDNF} neurons. *p<0.05, unpaired student's t-tests.

975 **(I-J)** The amplitude **(I)** and threshold **(J)** for the first AP firing at the holding voltage of -60mV
976 in control (black) and cKO (red) PVH^{BDNF} neurons. *p<0.05, unpaired student's t-tests.

977 **(K)** The cumulative fractions of mIPSC frequency were measured in control (black) and
978 cKO(red) PVH^{BDNF} neurons. The average frequency of events from a 2-minute stable recording
979 of each neuron is shown in the inset, unpaired student's t-tests.

980 **(L)** The cumulative fractions of mIPSC amplitude of control (black) and cKO (red) PVH^{BDNF}
981 neurons. The average amplitude of events from a 2-min stable recording of each neuron is
982 normalized to its capacitance and shown in the inset, unpaired student's t-tests.

983 **(M)** The area under the curve of each mIPSC event from a 2-minute recording is averaged.
984 Controls are shown in black, and cKOs are shown in red. unpaired t-tests, two-tailed. *p<0.05.

985 Data are shown as mean±SEM. Statistics: neuron numbers are in brackets (more than 3
986 mice/genotype)

987

988 **Figure 4: Selective *Rai1* ablation in PVH^{BDNF} neurons induces obesity**

989 **(A)** A schematic showing stereotaxic injection of adeno-associated viruses (AAVs) expressing
990 Cas9 protein and single-guide RNAs targeting *Rai1* (sgRai1) to delete *Rai1* from the PVH^{BDNF}
991 neurons of *Bdnf*$^{Cre/+}$ female mice. Scale bar = 50µm.

992 **(B)** Representative images showing that RAI1 immunoreactivity (cyan) was dramatically
993 reduced in *Bdnf*$^{Cre/+}$*; Ai9* mice injected with both sgRai1 and DIO-saCas9 viruses (Exp group n
994 =3, bottom row) into the PVH. In contrast, many PVH^{BDNF} neurons in *Bdnf*$^{Cre/+}$*; Ai9* mice
995 injected only with the sgRai1 virus showed RAI1 expression (Ctrl group n =3, top row).

996 **(C)** The percentage of PVH^{BDNF} neurons co-expressing RAI1 and GFP (virus) was significantly
997 reduced in the Exp group, indicating a successful *Rai1* deletion. unpaired t-test, two-tailed,
998 ****p<0.0001

999 **(D)** PVH^{BDNF} neuron-specific *Rai1* deletion induced body weight gain in Exp mice (Ctrl group:
1000 n=5, Exp group: n =5). Two-way ANOVA with Šidák's multiple comparisons test. *p<0.05,
1001 **p < 0.01, ****p < 0.0001.

1002 **(E)** Body composition was measured with Echo-MRI, showing an increased fat mass deposition
1003 in 26-week-old Exp mice. ns indicates the difference is not significant. Two-way ANOVA with
1004 Šidák's multiple comparisons test. ***p<0.001, ****p < 0.0001.

1005 **(F)** Fat deposition analysis shows that the Exp group has significantly more subcutaneous
1006 inguinal (S.C.ing) and epididymal white adipose tissue (eWAT) mass (grams). ns indicates the
1007 difference is not significant. Two-way ANOVA with Šidák's multiple comparisons test. *p<0.05,
1008 ****p < 0.0001.

1009 **(G)** Representative images showing eWAT adipocyte hypertrophy of the Exp group (left). Scale
1010 bar = 500µm. Frequency distribution of adipocytes at each cellular size (right). ns indicates not
1011 significantly different. Two-way ANOVA with Šidák's multiple comparisons test. *$p<0.05$,
1012 ***$p<0.001$.

1013 **(H)** Exp and control mice showed similar food intake. ns indicates not significantly different,
1014 unpaired t-test, two-tailed.

1015 **(I)** Blood leptin levels were significantly increased in the Exp mice. unpaired t-test, two-tailed,
1016 *$p<0.05$.

1017 **(J)** Exp and control mice showed similar energy expenditure. ns indicates the difference is not
1018 significant. Two-way ANOVA with Šidák's multiple comparisons test.

1019 **(K)** Exp mice showed reduced locomotor activity in the dark phase. ns indicates the difference is
1020 not significant. Two-way ANOVA with Šidák's multiple comparisons test. *$p<0.05$.

1021 **(L)** Exp mice became hyperglycemic during the glucose tolerance test. ns indicates the
1022 difference is not significant. Two-way ANOVA with Šidák's multiple comparisons test. *$p<0.05$.

1023 **(M)** Measurement of the area under the curve (AUC) in Exp and Ctrl mice during the glucose
1024 tolerance test. unpaired t-test, two-tailed, $p=0.05$.

1025 **(N)** Exp mice showed increased plasma insulin levels during the glucose tolerance test. Two-way
1026 ANOVA with Šidák's multiple comparisons test, **$p<0.01$.

1027 Data are shown as mean±SEM.

1028

1029 **Figure 5: LM22A-4 treatment partially alleviates obesity and stereotypic behaviour in**
1030 **adult SMS mice**

1031 **(A)** Representative western blot showing p-AKT, total AKT, Histone 3 (H3, a loading control)
1032 levels in the hypothalamus of saline-treated Ctrl, saline-treated SMS and LM22A-4-treated SMS
1033 mice.

1034 **(B)** Quantification showing deficits in p-AKT levels of the hypothalamus were reversed by
1035 LM22A-4 treatment in SMS mice. Unpaired t-test, two-tailed, *$p<0.05$.

1036 **(C-E)** Body weight of saline-injected control, saline-injected SMS, and LM22A-4 injected SMS
1037 mice. Saline or LM22A-4 treatment periods were highlighted in orange. ns indicates not
1038 significantly different. Two-way ANOVA with Šidák's multiple comparisons test. *$p<0.05$,
1039 **$p < 0.01$, ****$p < 0.0001$.

1040 **(F)** Food intake (in grams) of saline-injected control, saline-injected SMS, and LM22A-4
1041 injected SMS mice. ns indicates the difference is not significant. unpaired t-test, two-tailed,
1042 *$p<0.05$, **$p < 0.01$.

1043 **(G)** Locomotor activity (number of beam breaks) for saline-injected control, saline-injected
1044 SMS, and LM22A-4 injected SMS mice. ns indicates the difference is not significant. unpaired t-
1045 test, two-tailed, *$p<0.05$.

1046 **(H)** Fat deposition analysis shows that the saline-injected SMS group has significantly more
1047 subcutaneous inguinal (S.C.ing) and epididymal white adipose tissue (eWAT) mass (grams) than
1048 saline-injected Ctrl mice. S.C.ing and eWAT mass in LM22A-4 injected mice is comparable to
1049 the saline-injected mice. Two-way ANOVA with Šidák's multiple comparisons test. **$p < 0.01$,
1050 ***$p<0.001$, ****$p < 0.0001$.

1051 **(I)** High-density lipoprotein (HDL) levels were restored to normal in LM22A-4 injected SMS
1052 mice. ns indicates the difference is not significant. unpaired t-test, two-tailed, **$p < 0.01$,
1053 ***$p<0.001$.

1054 **(J)** Insulin levels in saline-injected control, saline-injected SMS, and LM22A-4 injected SMS
1055 mice right before the start of the insulin tolerance test (time point 0). ns indicates the difference
1056 is not significant. unpaired t-test, two-tailed, *$p<0.05$.

1057 **(K)** Insulin tolerance test performed on saline-injected control, saline-injected SMS, and
1058 LM22A-4 injected SMS mice, two weeks post daily administration of LM22A-4 or saline, shows
1059 reductions in the blood glucose levels of LM22A-4 treated SMS mice. * Shows significance
1060 between saline-injected Ctrl and saline-injected SMS group. ns indicates the difference is not
1061 significant. Two-way ANOVA with Šidák's multiple comparisons test. **$p < 0.01$.

1062 **(L)** Stereotypic rearing behaviour was fully rescued in LM22A-4 treated SMS mice. ns indicates
1063 the difference is not significant. unpaired t-test, two-tailed. *$p<0.05$, **$p < 0.01$.

1064 Data are shown as mean±SEM.

1065

1066

1067

1068

1069

1070 **Fig 1-figure supplement 1: Differentially expressed proteins in the hypothalamus of SMS**
1071 **mice**

1072 A heat map showing hierarchical clustering of differentially expressed proteins in the
1073 hypothalamus of SMS mice.

1074

1075

1076 **Fig 2-figure supplement 1: The *Bdnf*^{Cre} allele labels BDNF-producing neurons in the**
1077 **paraventricular nucleus of the hypothalamus**

1078 **(A)** Schematic showing a transgenic mouse expressing *Bdnf*^{Cre}-dependent td-Tomato (Ai9)
1079 signals in BDNF-expressing cells.

1080 **(B-E)** Colocalization of *Bdnf*^{Cre}-dependent td-Tomato signals with endogenous BDNF protein.
1081 Black: DAPI, Magenta: BDNF-producing cells; Green: endogenous BDNF. Scale bar: 50 µm,
1082 yellow arrowheads indicate Ai9 marked BDNF cells coexpressing endogenous BDNF.

1083

1084

1085 **Fig 2-figure supplement 2: RAI1 expression in BDNF-expressing but not oxytocin-**
1086 **expressing magnocellular PVH neurons**

1087 **(A-H)** Representative images of DAPI expression (blue, **A**), oxytocin (green, **B**), BDNF-
1088 producing cells (Ai9 reporter, magenta, **C**), and RAI1 protein (cyan, **D**) in the PVH. Note that
1089 BDNF-producing neurons are distinct from the oxytocin-expressing neurons (**E**) and that RAI1 is
1090 more selectively expressed in the BDNF-expressing neurons (**F-H**).

1091 **(I)** Quantification showing the percentage of RAI1^{+} cells that co-express either BDNF (left bar,
1092 magenta) or oxytocin (right bar, green) in the PVH. n=3 mice/group. Data are shown as
1093 mean±SEM.

1094

1095

1096 **Fig 2-figure supplement 3: Ablating *Rai1* from the BDNF-producing cells induces body**
1097 **weight gain and defective energy homeostasis**

1098 **(A)** Schematic representation of the conditional knockout mice carrying either normal *Rai1*
1099 alleles and the Ai9 reporter in BDNF-producing cells (top) or homozygous *Rai1* deletion and the
1100 Ai9 reporter in the BDNF-producing cells.

1101 **(B)** Representative images showing the expression of DAPI (white), RAI1-expressing cells
1102 (green), and BDNF-expressing cells (Ai9 reporter, magenta) in the PVH. The top panel shows
1103 the Ctrl group with RAI1-Ai9 co-expression (yellow arrowheads) and the bottom panel shows
1104 reduced RAI1 and Ai9 colocalization (yellow arrowheads). Note that RAI1 expression was still
1105 detected in non-BDNF neurons in the PVH.

1106 **(C)** Quantification showing the percentage of BDNF-producing cells was not altered by *Rai1*
1107 deletion, indicating that RAI1 loss did not impair the generation or survival of PVH^{BDNF} neurons.
1108 ns indicates not significantly different, unpaired t-test, two-tailed.

1109 **(D)** The $Bdnf^{Cre/+}$ and $Bdnf^{Cre/+}$; $Rai1^{fl/+}$ female mice had similar body weights. ns indicates not
1110 significantly different. Two-way ANOVA with Šidák's multiple comparisons test.

1111 **(E-G)** Blood parameter analysis of triglycerides (TG), high-density lipoprotein (HDL), low-
1112 density lipoprotein and very low-density lipoprotein (LDL+VLDL) did not differ between Ctrl
1113 and cKO mice. ns indicates not significantly different, unpaired t-test, two-tailed.

1114 **(H)** The respiratory exchange rate did not differ between Ctrl and cKO mice. ns indicates the
1115 difference is not significant. Two-way ANOVA with Šidák's multiple comparisons test.

1116 **(I)** In the glucose tolerance test, the cKO mice showed an increased area under the curve (AUC).
1117 ***$p<0.001$, unpaired t-test, two-tailed.

1118 **(J)** In the glucose tolerance test, cKO mice showed increased insulin levels at the beginning of
1119 the test and 30 minutes after glucose administration. ns indicates the difference is not significant.
1120 Two-way ANOVA with Šidák's multiple comparisons tests, *$p < 0.05$, **$p<0.01$.

1121

1122 **(K)** In the insulin tolerance test, blood glucose level is measured after insulin injection. ns
1123 indicates the difference is not significant. Two-way ANOVA with Šidák's multiple comparisons
1124 test, *p < 0.05.

1125 Data are shown as mean±SEM.

1126

1127

1128

1129 **Fig 2-figure supplement 4: Metabolic profiles of male cKO mice lacking RAI1 expression in**
1130 **the BDNF-producing cells**

1131 **(A)** Male cKO mice gained significantly more weight than Ctrl mice beginning at 15 weeks of
1132 age. Two-way ANOVA with Šidák's multiple comparisons test, *p < 0.05, **p<0.01,
1133 ****p < 0.0001.

1134 **(B)** Male *Bdnf*$^{Cre/+}$ and *Bdnf*$^{Cre/+}$; *Rai1*$^{fl/+}$ mice had similar body weights. ns indicates the
1135 difference is not significant. Two-way ANOVA with Šidák's multiple comparisons test.

1136 **(C)** Echo-MRI analysis showed that 26-week-old male cKO mice had a significantly increased
1137 body weight due to increased fat but not lean mass. ns indicates the difference is not significant.
1138 unpaired t-test, two-tailed, **p<0.01, ****p<0.0001.

1139 **(D)** Fat disposition analysis showing the weight of brown adipocytes (BAT), subcutaneous
1140 inguinal (S.C.ing), and epididymal white adipose tissues (eWAT). ns indicates the difference is
1141 not significant. unpaired t-test, two-tailed, *p<0.05, **p<0.01.

1142 **(E)** Male cKO mice showed eWAT cell hypertrophy. Top: Representative images of the eWAT
1143 tissues in Ctrl and cKO mice. Scale bar = 500μm. Bottom: Frequency distribution of cellular
1144 sizes. Two-way ANOVA with Šidák's multiple comparisons test, *p < 0.05, **p<0.01,
1145 ***p<0.001, ****p < 0.0001.

1146 **(F-I)** Blood parameter analysis showing that male cKO mice showed significantly increased
1147 leptin levels **(F)** without alterations in TG **(G)**, HDL **(H)**, and LDL+VLDL **(I)**. ns indicates the
1148 difference is not significant. unpaired t-test, two-tailed. *p< 0.05.

1149 **(J)** No differences were found in the respiratory exchange rate in male Ctrl and cKO mice. ns
1150 indicates the difference is not significant. Two-way ANOVA with Šidák's multiple comparisons
1151 test.

1152 **(K)** Male cKO mice showed a significantly increased food intake compared to Ctrl littermates.,
1153 unpaired t-test, two-tailed, *p< 0.05.

1154 **(L)** Male cKO mice showed increased energy expenditure at the dark phase. ns indicates the
1155 difference is not significant. Two-way ANOVA with Šidák's multiple comparisons test, *p<0.05.

1156 **(M)** Male Ctrl and cKO mice showed similar locomotor activities. ns indicates the difference is
1157 not significant. Two-way ANOVA with Šidák's multiple comparisons test.

1158 **(N-P)** Glucose tolerance test shows that cKO male mice are glycemic 45 minutes post
1159 intraperitoneal glucose administration **(N)** and had increased AUC (unpaired t-test, two-tailed)
1160 **(O)**, despite significantly higher insulin levels before and 30 minutes after glucose administration
1161 **(P)**, suggesting potential insulin insensitivity. ns indicates the difference is not significant. Two-
1162 way ANOVA with Šidák's multiple comparisons tests, *p<0.05, **p < 0.01, ***p<0.001.

1163 **(Q)** Insulin tolerance test showing that male cKO mice showed significantly higher blood
1164 glucose levels 60 minutes after intraperitoneal insulin administration. Two-way ANOVA with
1165 Šidák's multiple comparisons test, *p<0.05, **p < 0.01.

1166 Data are shown as mean±SEM.

1167

1168 **Fig 3-figure supplement 1: The cellular and synaptic properties of control and *Rai1*-**
1169 **deficient PVH^{BDNF} neurons**

1170 **(A)** Representative traces of rebound and rebound repetitive firing of PVH^{BDNF} neurons in
1171 control (black) and cKO (red).

1172 **(B)** Representative AP waveforms at holding voltages of -80mV, -60mV, and -50mV in control
1173 (left) and -50mV and -45mV in cKO (right).

1174 **(C)** The half-width of AP initiated at a holding voltage of -60mV (neuronal numbers in brackets,
1175 ns indicates the difference is not significant, unpaired t-test, two-tailed).

1176 **(D)** Representative traces of miniature recordings in control (black) and cKO (red) PVH^{BDNF}
1177 neurons. The traces were recorded with a Cs-based internal at a holding voltage of -70mV in
1178 aCSF (top), spontaneous mEPSCs were recorded in aCSF containing 1uM TTX at a holding
1179 voltage of -70mV (middle), and mIPSCs were recorded at holding voltage of +10mV (bottom).

1180 **(E)** Quantification showing that the cellular size of cKO PVH^{BDNF} neurons was significantly
1181 smaller than Ctrl neurons. unpaired t-test, two-tailed. ****$p<0.0001$.

1182

1183

1184 **Fig 4-figure supplement 1: Metabolic profile of mice lacking *Rai1* in PVH^{BDNF} neurons**

1185 **(A)** Representative images showing co-expression of virus-infected cells (GFP/green), $Bdnf^{Cre}$-
1186 dependent Ai9 signals (BDNF cells, magenta), and endogenous RAI1 (cyan). Yellow arrowheads
1187 indicate BDNF neurons infected with AAV and in these cells, RAI1 signals were diminished in
1188 Exp but not Ctrl mice. Scale bar = 50µm.

1189 **(B-C)** The total number of PVH^{BDNF} neurons **(B)** and total number of PVH^{BDNF} neurons infected
1190 with AAVs **(C)** per slice show that *Rai1* deletion or virus infection did not alter the total number
1191 of PVH^{BDNF} neurons. ns indicates the difference is not significant. unpaired t-test, two-tailed.

1192 **(D)** *Rai1* expression was significantly reduced in PVH^{BDNF} neurons infected with both AAVs
1193 compared to PVH^{BDNF} neurons infected with sgRai1-GFP AAV alone. unpaired t-test, two-tailed,
1194 **$p<0.01$.

1195 **(E)** The number of PVH^{BDNF} neurons that co-express RAI1 was significantly reduced in the Exp
1196 group. unpaired t-test, unpaired, **$p<0.01$.

1197 **(F)** Representative image showing lack of viral expression in the PVH neighbouring nuclei.
1198 ARC: arcuate nucleus. VMH: ventromedial nucleus of the hypothalamus. 3V: third ventricle.
1199 Scale bar = 50µm.

1200 (**G**) The respiratory exchange rate remained similar in Ctrl and Exp mice. ns indicates the
1201 difference is not significant. Two-way ANOVA, Šídák's multiple comparisons test.

1202 **(H-J)** Blood parameter analysis showing TG, HDL, and LDL+VLDL levels were similar in Ctrl
1203 and Exp mice. ns indicates the difference is not significant. unpaired t-test, two-tailed.

1204 **(K)** In the insulin tolerance test, the Exp group showed a trend towards increased blood glucose
1205 levels after insulin injection. Two-way ANOVA, Šídák's multiple comparisons test.

1206 Data are shown as mean±SEM.

1207

1208

1209 **Figure 5—figure supplement 1: LM22A-4 treatment does not disrupt energy homeostasis**
1210 **and repetitive rearing in the Ctrl mice**

1211 **(A)** LM22A-4 concentration in the hypothalamus and forebrain of SMS mice 1 hour (black dots)
1212 and 3 hours (red dots) after simultaneous intranasal and IP injections.

1213 **(B)** Four independent sets of western blotting analyses showing reduced p-AKT levels in the
1214 hypothalamus of saline-treated SMS mice, which were increased by LM22A-4 treatment. Total
1215 AKT protein was used as a control.

1216 **(C)** Similar body weight of Ctrl mice treated with either saline or LM22A-4. ns indicates the
1217 difference is not significant. Two-way ANOVA, Šídák's multiple comparisons test.

1218 **(D)** Energy expenditure was not different between groups in the light vs. dark phase. ns indicates
1219 the difference is not significant. Two-way ANOVA, Šídák's multiple comparisons test.

1220 **(E)** Respiratory exchange rates were not different between groups in the light vs. dark phase. ns
1221 indicates the difference is not significant. Two-way ANOVA, Šídák's multiple comparisons test.

1222 **(F)** Repetitive rearing behaviour in Ctrl mice was not altered by LM22A-4 treatment. ns
1223 indicates the difference is not significant. unpaired t-test, two-tailed.

1224 Data are shown as mean±SEM.

1225

1226

1227 **Figure 5—figure supplement 2: LM22A-4 treatment in adult SMS mice is insufficient to**
1228 **improve social interaction deficit**

1229 **(A)** Schematic showing the tube test that assesses social interaction between stranger mice of
1230 different genotypes.

1231 **(B)** 7-week-old Ctrl mice won significantly more than SMS mice before the LM22A-4 treatment.
1232 unpaired t-test, two-tailed. ****$p<0.0001$.

1233 **(C)** 10-week-old saline-injected Ctrl mice won significantly more than the saline-injected SMS
1234 mice (two weeks post-LM22A-4 treatment). unpaired t-test, two-tailed, ***$p<0.001$.

1235 **(D)** 10-week-old saline-injected Ctrl mice won significantly more than LM22A-4 injected SMS
1236 mice. unpaired t-test, two-tailed, *$p<0.05$.

1237 **(E)** 10-week-old saline-injected SMS mice showed a similar winning rate to LM22A-4-injected
1238 SMS mice. ns indicates the difference is not significant. unpaired t-test, two-tailed.

1239 Data are shown as mean±SEM.

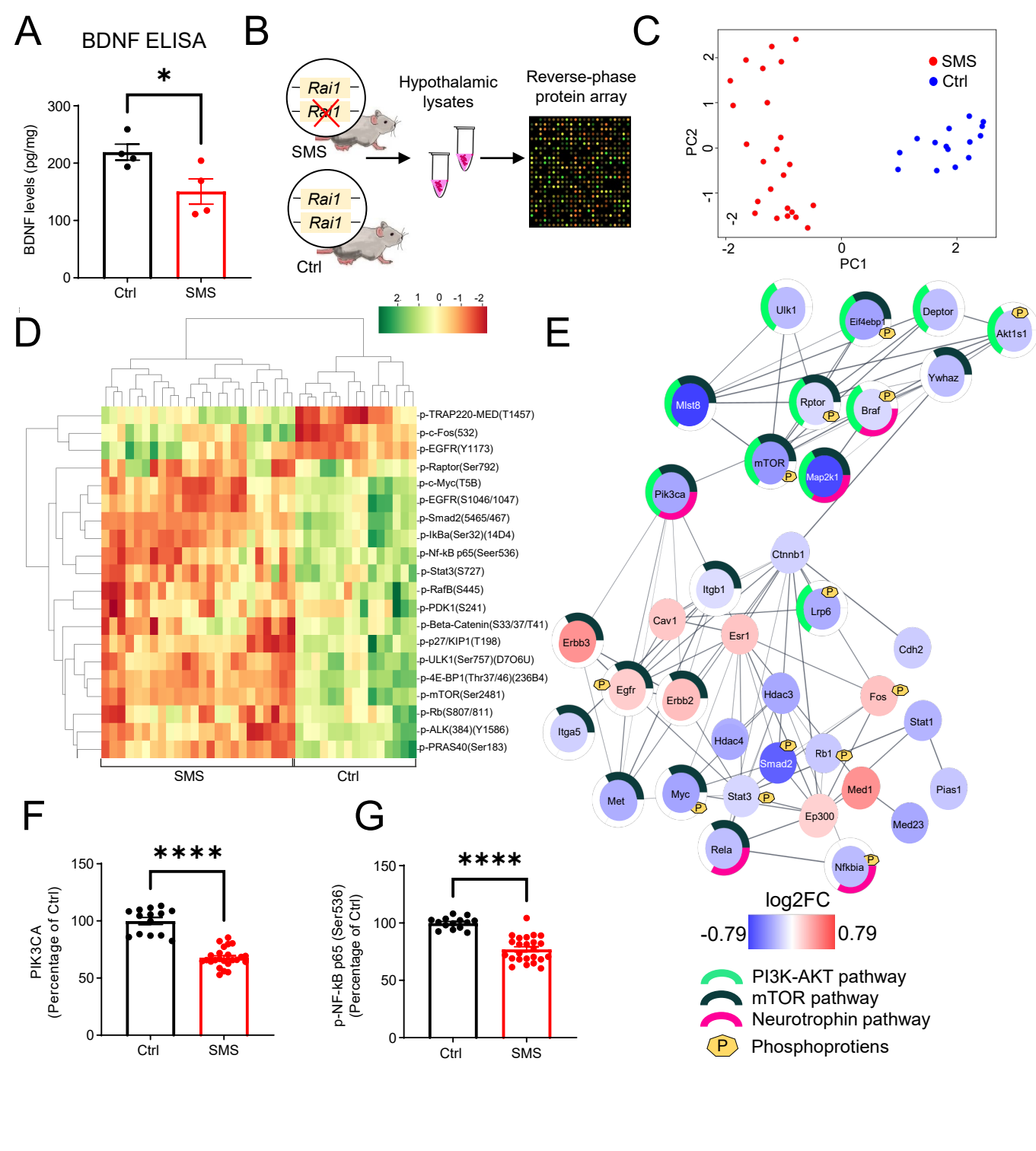
A
BDNF ELISA
*
BDNF levels (pg/mg)
300
200
100
0
Ctrl
SMS
B
Rai1
Rai1
SMS
Rai1
Rai1
Ctrl
Hypothalamic lysates
Reverse-phase protein array
C
SMS
Ctrl
PC2
PC1
2
1
0
-1
-2
D
2
1
0
-1
-2
p-TRAP220-MED(T1457)
p-c-Fos(532)
p-EGFR(Y1173)
p-Raptor(Ser792)
p-c-Myc(T5B)
p-EGFR(S1046/1047)
p-Smad2(5465/467)
p-IkBa(Ser32)(14D4)
p-Nf-kB p65(Seer536)
p-Stat3(S727)
p-RafB(S445)
p-PDK1(S241)
p-Beta-Catenin(S33/37/T41)
p-p27/KIP1(T198)
p-ULK1(Ser757)(D7O6U)
p-4E-BP1(Thr37/46)(236B4)
p-mTOR(Ser2481)
p-Rb(S807/811)
p-ALK(384)(Y1586)
p-PRAS40(Ser183)
SMS
Ctrl
E
Ulk1
Eif4ebp1
Deptor
Akt1s1
Ywhaz
Mlst8
Rptor
Braf
mTOR
Map2k1
Pik3ca
Ctnnb1
Itgb1
Lrp6
Cav1
Esr1
Erbb3
Cdh2
Egfr
Erbb2
Hdac3
Fos
Stat1
Itga5
Hdac4
Smad2
Rb1
Med1
Pias1
Met
Myc
Stat3
Ep300
Med23
Rela
Nfkbia
P
log2FC
-0.79
0.79
PI3K-AKT pathway
mTOR pathway
Neurotrophin pathway
Phosphoprotiens
F
****
PIK3CA (Percentage of Ctrl)
150
100
50
0
Ctrl
SMS
G
****
p-NF-kB p65 (Ser536) (Percentage of Ctrl)
150
100
50
0
Ctrl
SMS

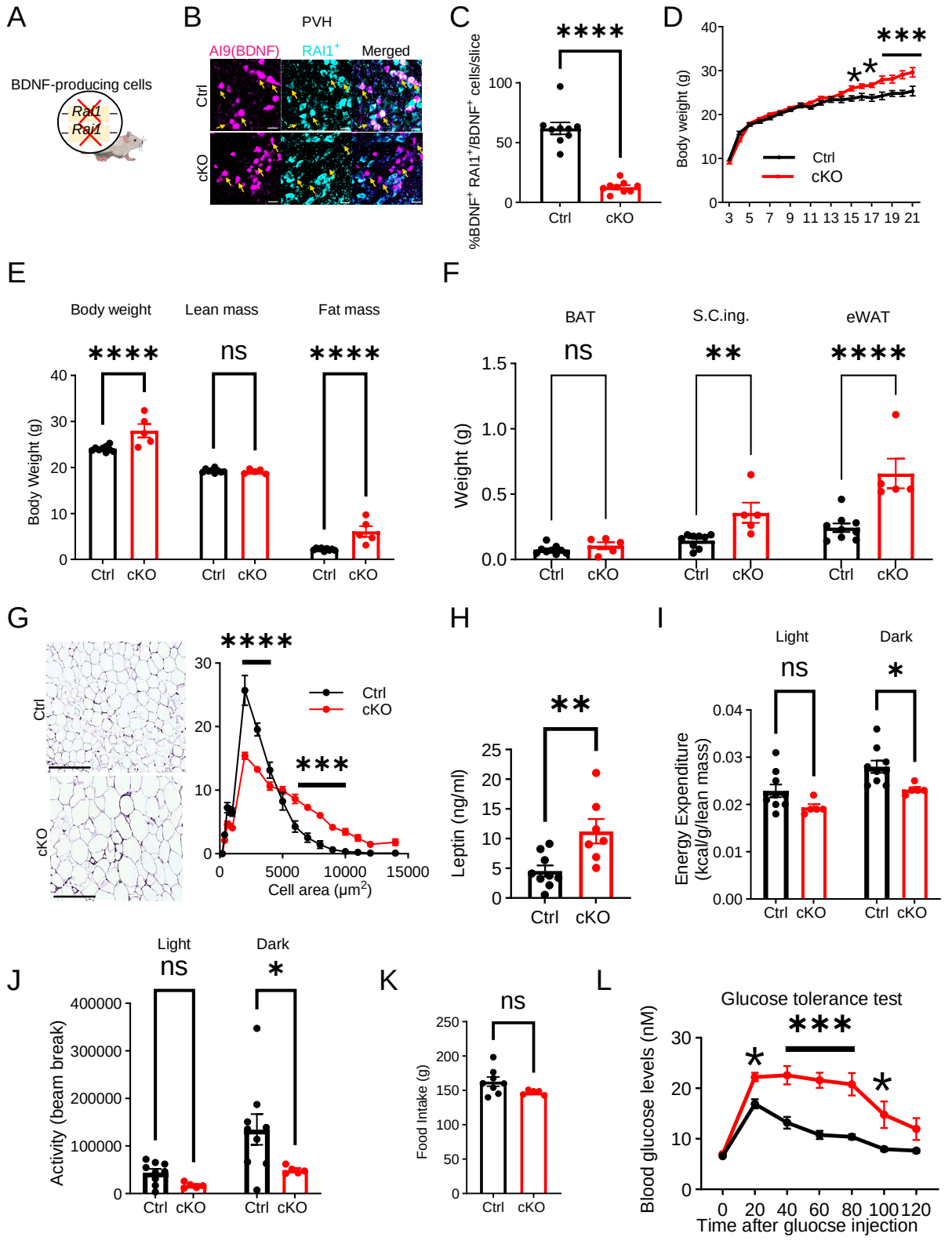
A
BDNF-producing cells
Ral1
Ral1
B
PVH
AI9(BDNF)
RAI1+
Merged
Ctrl
cKO
C
****
%BDNF+ RAI1+/BDNF+ cells/slice
100
50
0
Ctrl
cKO
D
***
**
Body weight (g)
40
30
20
10
0
Ctrl
cKO
3 5 7 9 11 13 15 17 19 21
E
Body weight
Lean mass
Fat mass
****
ns
****
Body Weight (g)
40
30
20
10
0
Ctrl cKO Ctrl cKO Ctrl cKO
F
BAT
S.C.ing.
eWAT
ns
**
****
Weight (g)
1.5
1.0
0.5
0.0
Ctrl cKO Ctrl cKO Ctrl cKO
G
Ctrl
cKO
****
***
Ctrl
cKO
30
20
10
0
0 5000 10000 15000
Cell area (μm2)
H
**
Leptin (ng/ml)
25
20
15
10
5
0
Ctrl cKO
I
Light
Dark
ns
*
Energy Expenditure (kcal/g/lean mass)
0.04
0.03
0.02
0.01
0.00
Ctrl cKO Ctrl cKO
J
Light
Dark
ns
*
Activity (beam break)
400000
300000
200000
100000
0
Ctrl cKO Ctrl cKO
K
ns
Food Intake (g)
250
200
150
100
50
0
Ctrl cKO
L
Glucose tolerance test
***
*
*
Blood glucose levels (nM)
30
20
10
0
0 20 40 60 80 100 120
Time after gluocse injection

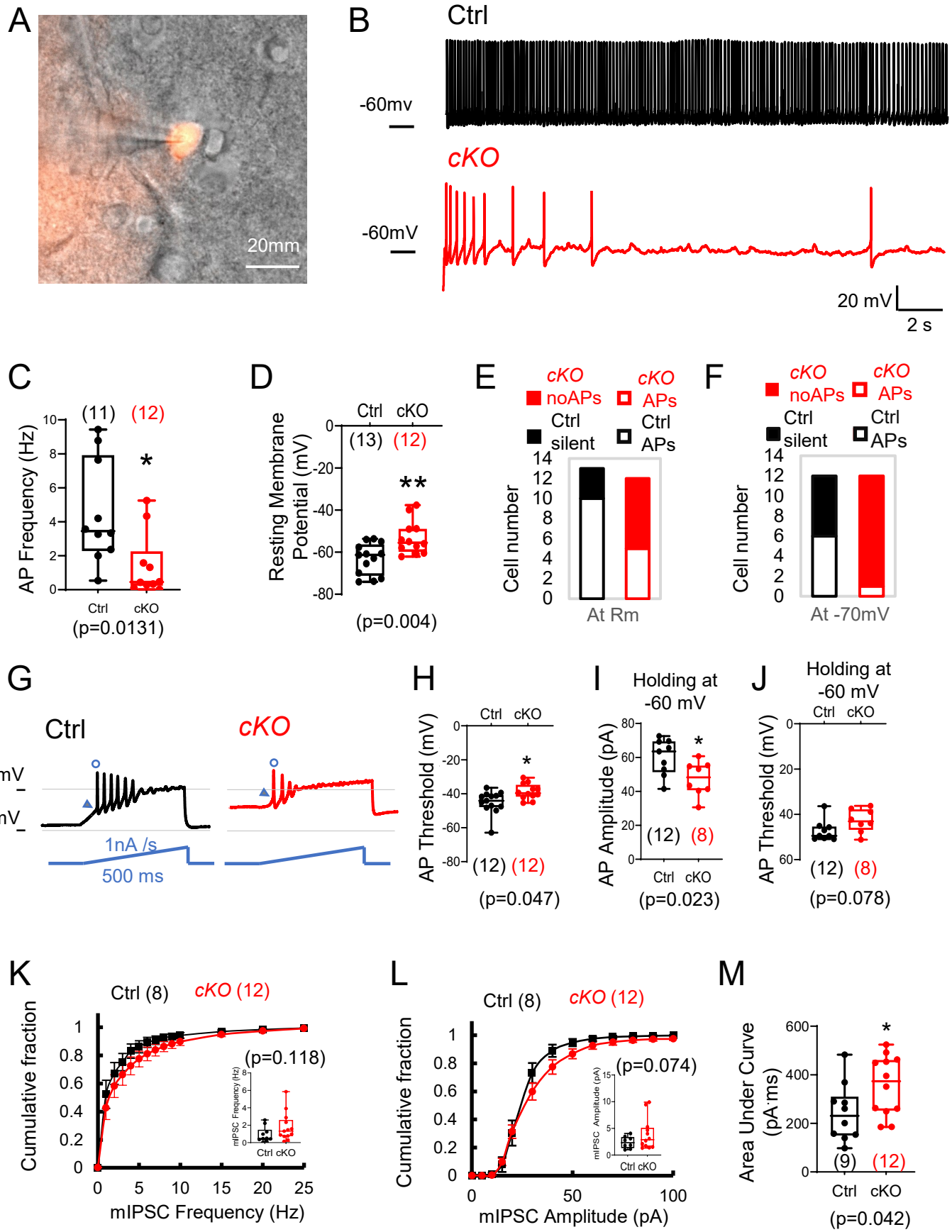
A
20mm
B
Ctrl
-60mv
cKO
-60mV
20 mV
2 s
C
AP Frequency (Hz)
(11)
(12)
*
Ctrl
cKO
(p=0.0131)
D
Resting Membrane Potential (mV)
Ctrl
cKO
(13)
(12)
**
(p=0.004)
E
cKO noAPs
cKO APs
Ctrl silent
Ctrl APs
Cell number
At Rm
F
cKO noAPs
cKO APs
Ctrl silent
Ctrl APs
Cell number
At -70mV
G
Ctrl
cKO
-40mV
-60mV
1nA /s
500 ms
H
AP Threshold (mV)
Ctrl
cKO
*
(12)
(12)
(p=0.047)
I
Holding at -60 mV
AP Amplitude (pA)
*
(12)
(8)
Ctrl
cKO
(p=0.023)
J
Holding at -60 mV
AP Threshold (mV)
Ctrl
cKO
(12)
(8)
(p=0.078)
K
Ctrl (8)
cKO (12)
Cumulative fraction
(p=0.118)
mIPSC Frequency (Hz)
L
Ctrl (8)
cKO (12)
Cumulative fraction
(p=0.074)
mIPSC Amplitude (pA)
M
Area Under Curve (pA·ms)
*
(9)
(12)
Ctrl
cKO
(p=0.042)

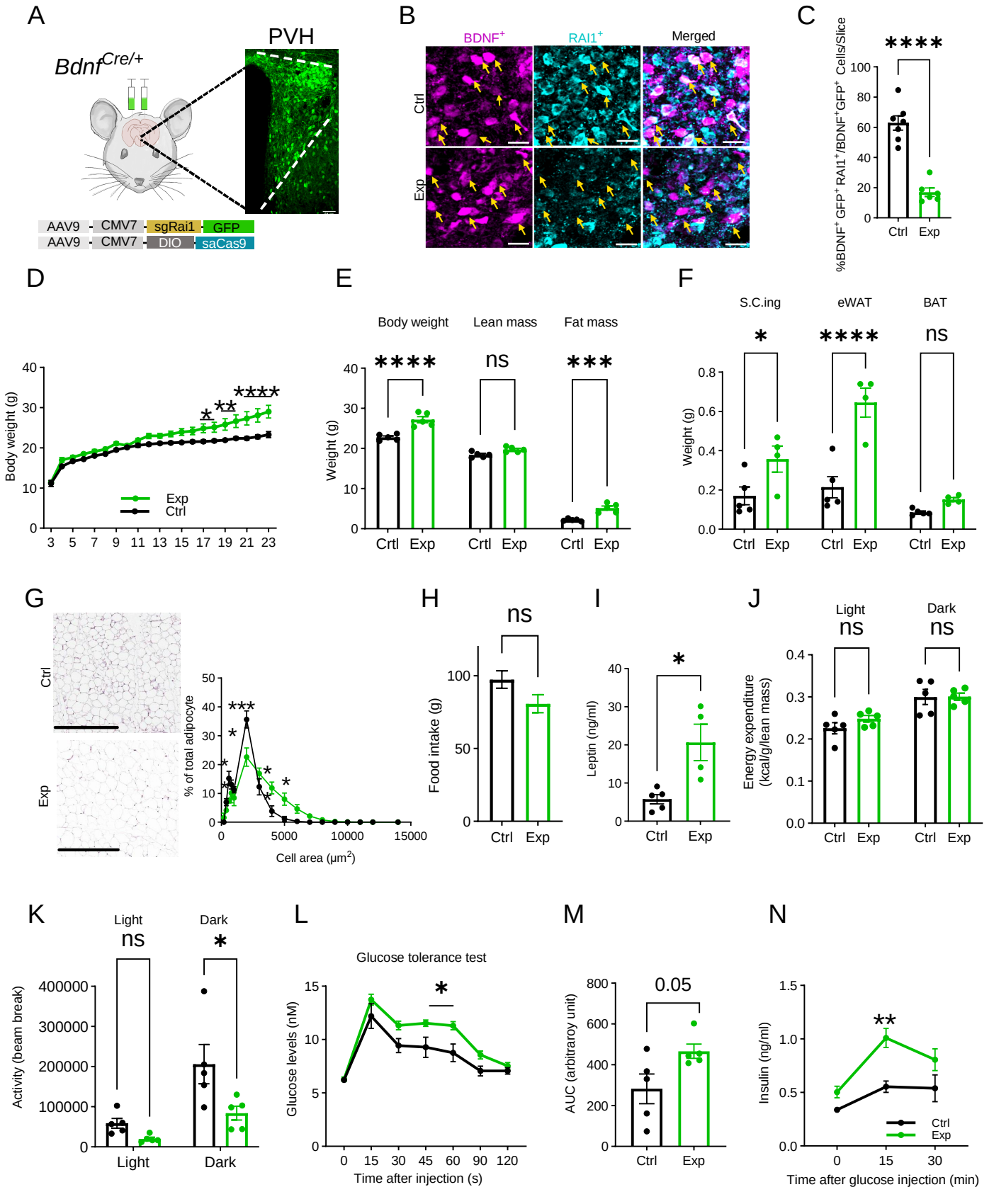
A
Bdnf Cre/+
PVH
AAV9 - CMV7 - sgRai1 - GFP
AAV9 - CMV7 - DIO - saCas9
B
BDNF+
RAI1+
Merged
Ctrl
Exp
C
%BDNF+ GFP+ RAI1+/BDNF+GFP+ Cells/Slice
****
Ctrl
Exp
D
Body weight (g)
Exp
Ctrl
E
Body weight
Lean mass
Fat mass
Weight (g)
****
ns
***
Crtl
Exp
F
S.C.ing
eWAT
BAT
Weight (g)
*
****
ns
Ctrl
Exp
G
Ctrl
Exp
% of total adipocyte
Cell area (μm2)
H
ns
Food intake (g)
I
*
Leptin (ng/ml)
J
Light
Dark
ns
ns
Energy expenditure (kcal/g/lean mass)
K
Light
Dark
ns
*
Activity (beam break)
L
Glucose tolerance test
*
Glucose levels (nM)
Time after injection (s)
M
0.05
AUC (arbitraroy unit)
N
**
Insulin (ng/ml)
Ctrl
Exp
Time after glucose injection (min)

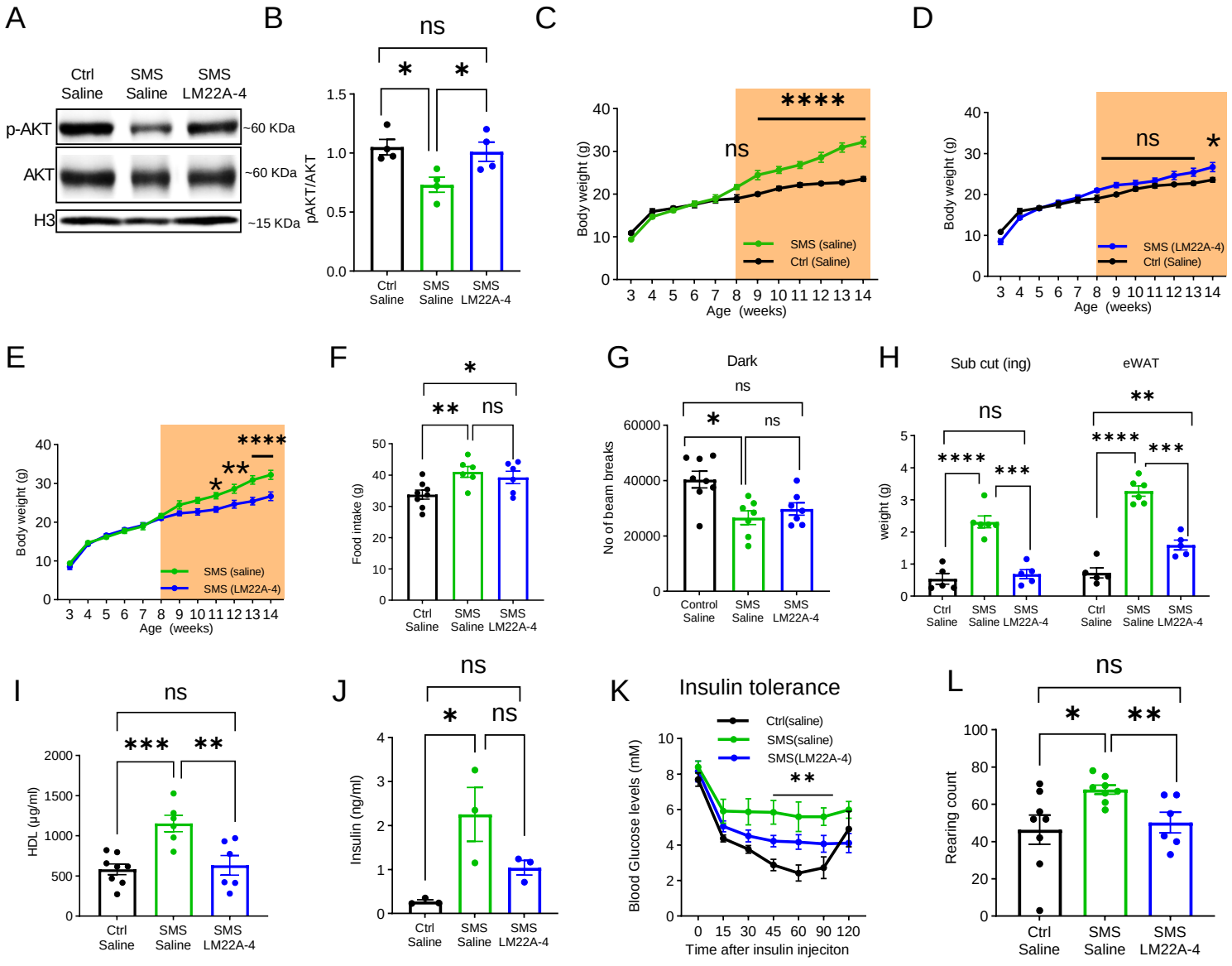
A
Ctrl Saline
SMS Saline
SMS LM22A-4
p-AKT
AKT
H3
~60 KDa
~60 KDa
~15 KDa
B
ns
*
*
pAKT/AKT
1.5
1.0
0.5
0.0
Ctrl Saline
SMS Saline
SMS LM22A-4
C
****
ns
Body weight (g)
SMS (saline)
Ctrl (Saline)
Age (weeks)
D
ns
*
Body weight (g)
SMS (LM22A-4)
Ctrl (Saline)
Age (weeks)
E
****
**
*
Body weight (g)
SMS (saline)
SMS (LM22A-4)
Age (weeks)
F
*
**
ns
Food intake (g)
Ctrl Saline
SMS Saline
SMS LM22A-4
G
Dark
ns
*
ns
No of beam breaks
Control Saline
SMS Saline
SMS LM22A-4
H
Sub cut (ing)
eWAT
ns
****
***
**
****
***
weight (g)
Ctrl Saline
SMS Saline
SMS LM22A-4
I
ns
***
**
HDL (μg/ml)
Ctrl Saline
SMS Saline
SMS LM22A-4
J
ns
*
ns
Insulin (ng/ml)
Ctrl Saline
SMS Saline
SMS LM22A-4
K
Insulin tolerance
Ctrl(saline)
SMS(saline)
SMS(LM22A-4)
**
Blood Glucose levels (mM)
Time after insulin injeciton
L
ns
*
**
Rearing count
Ctrl Saline
SMS Saline
SMS LM22A-4

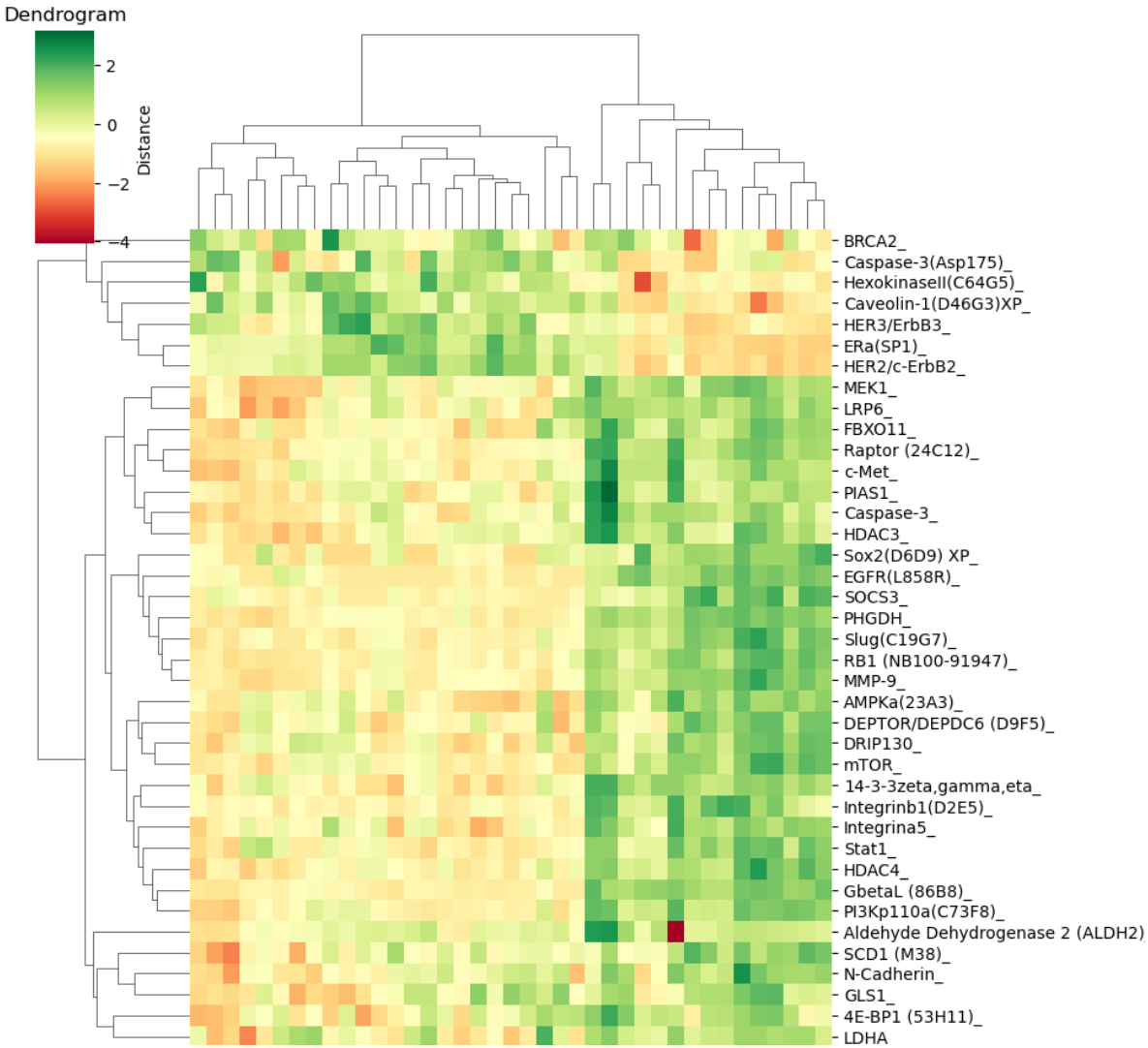

Figure 1—figure supplement 1

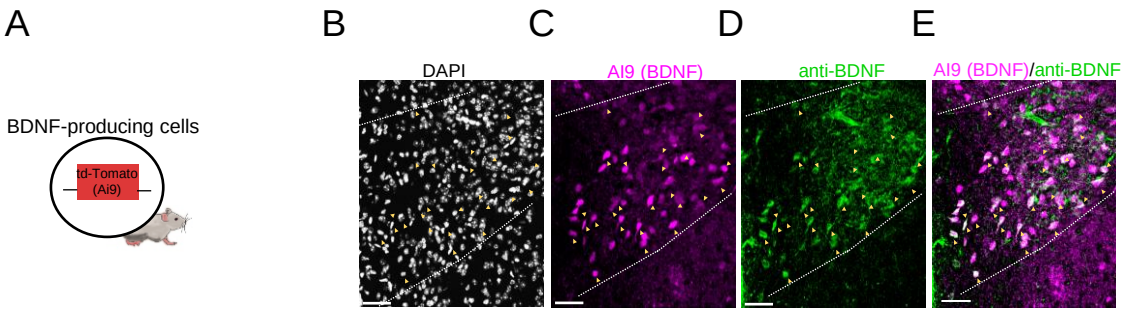

Figure 2—figure supplement 1

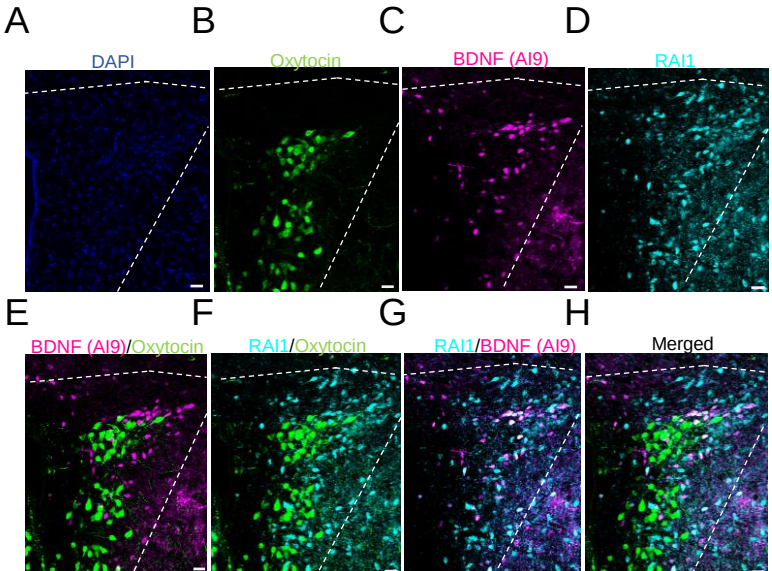

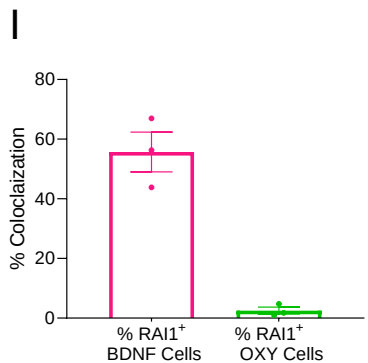

Figure 2—figure supplement 2

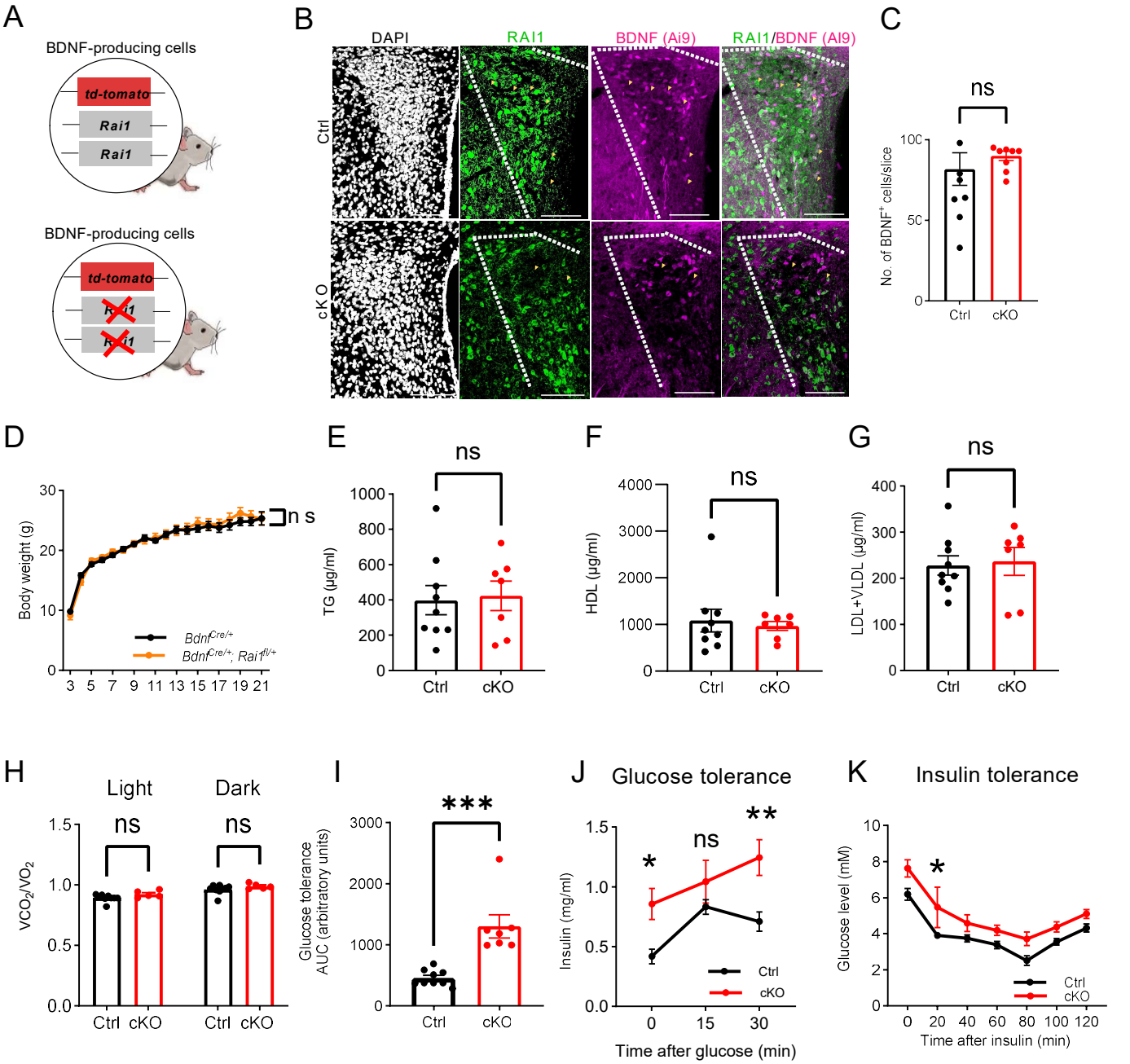

Fig 2-figure supplement 3

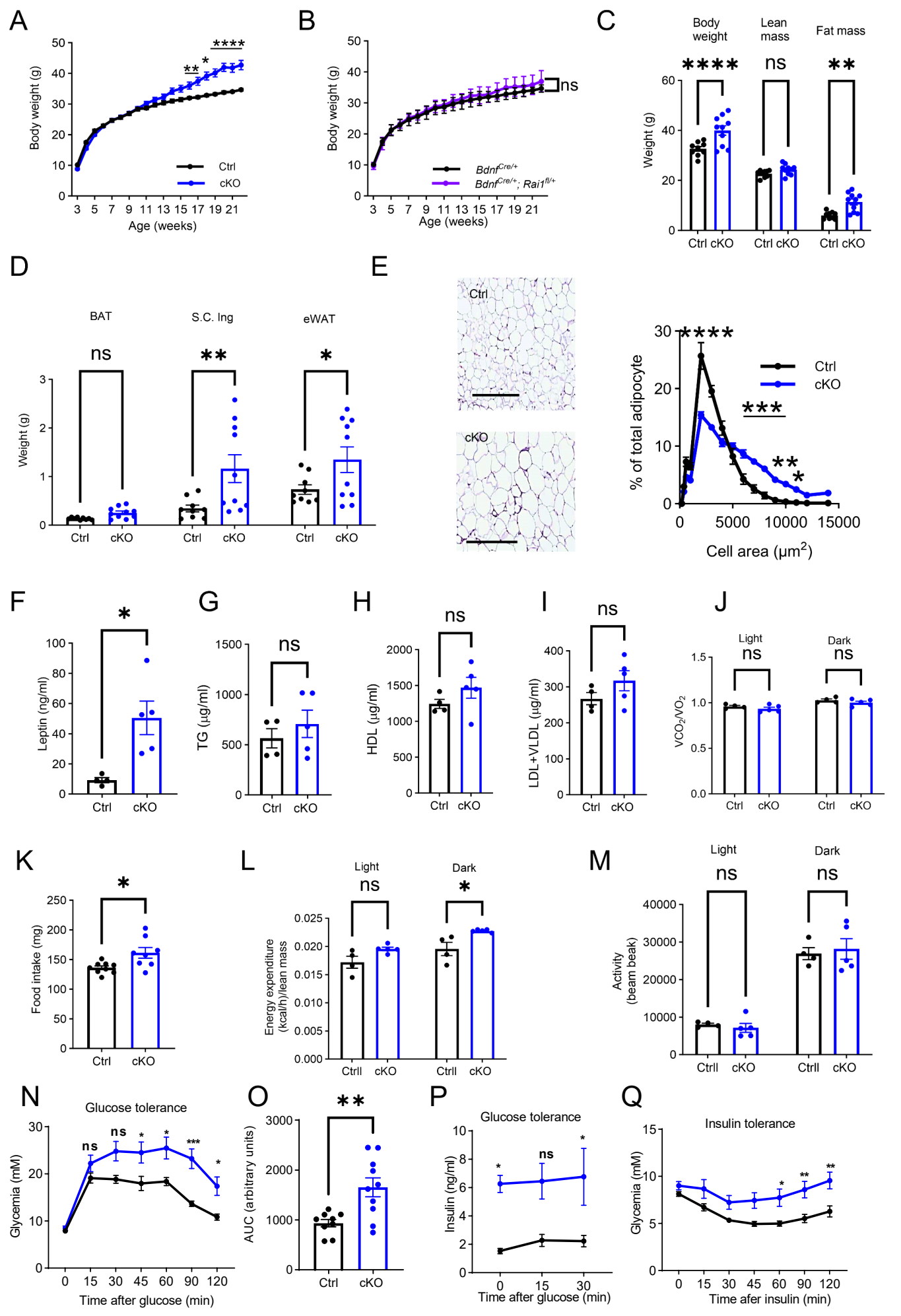

Fig 2-figure supplement 4

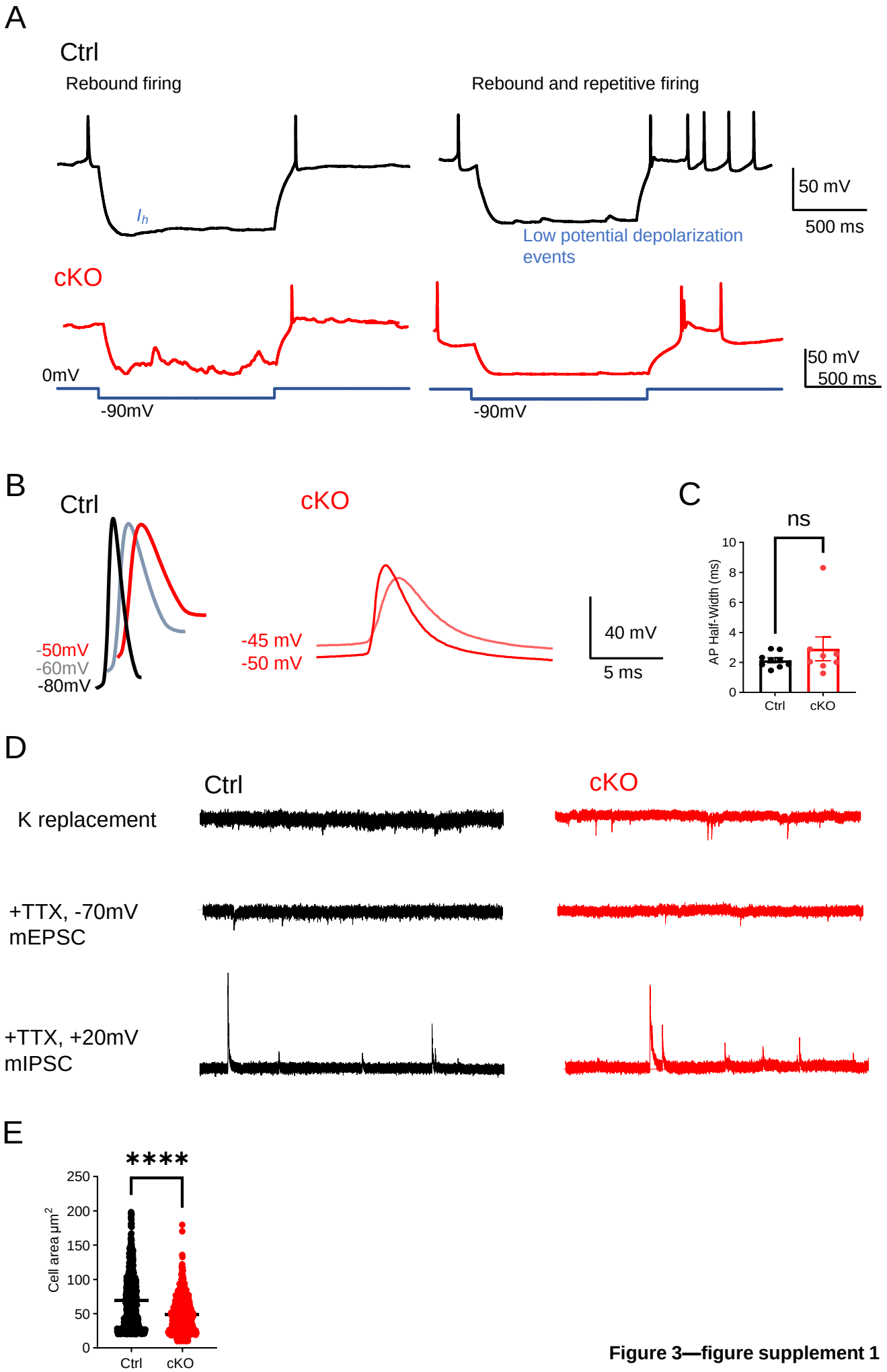

Figure 3—figure supplement 1

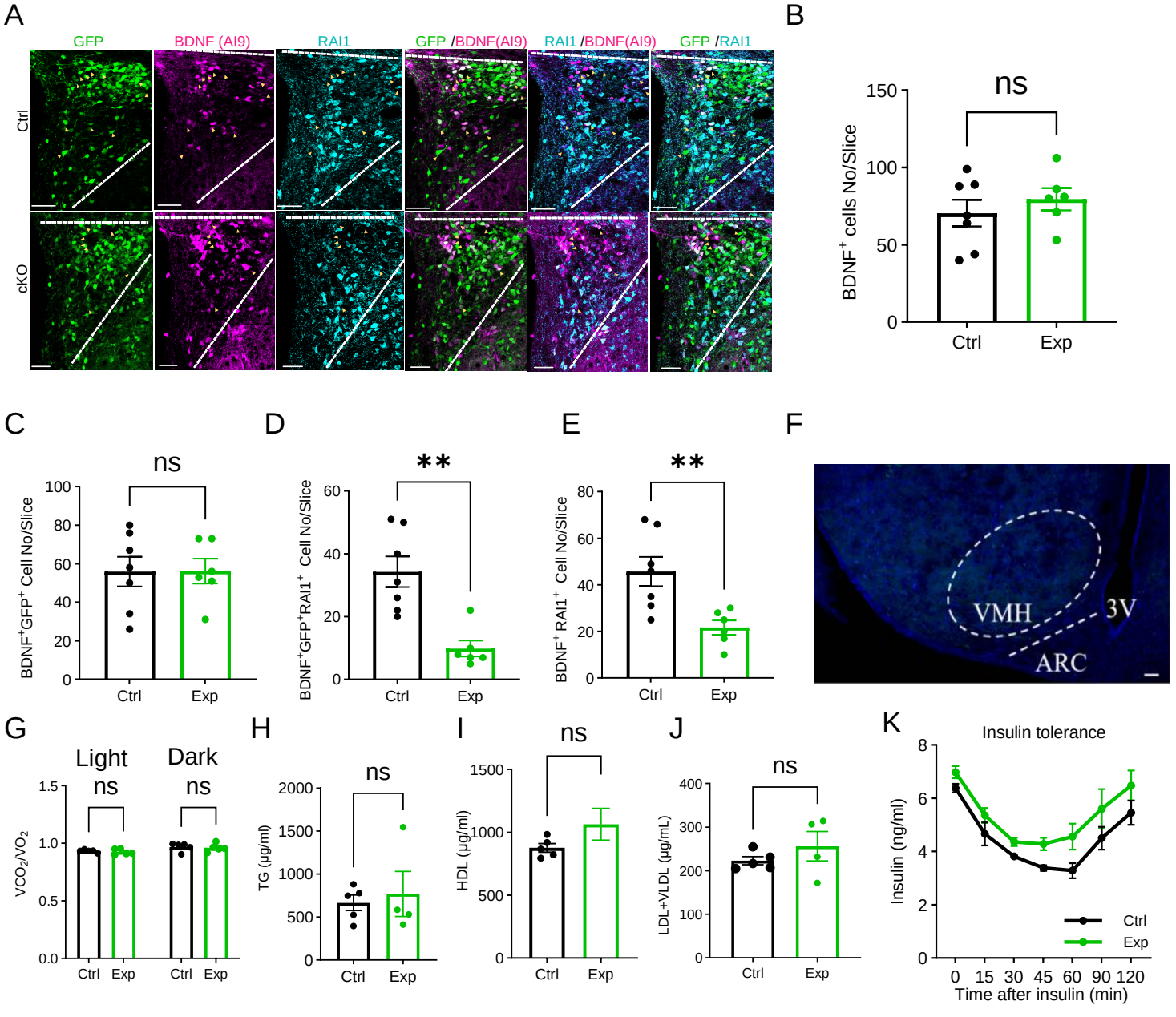

Figure 4—figure supplement 1

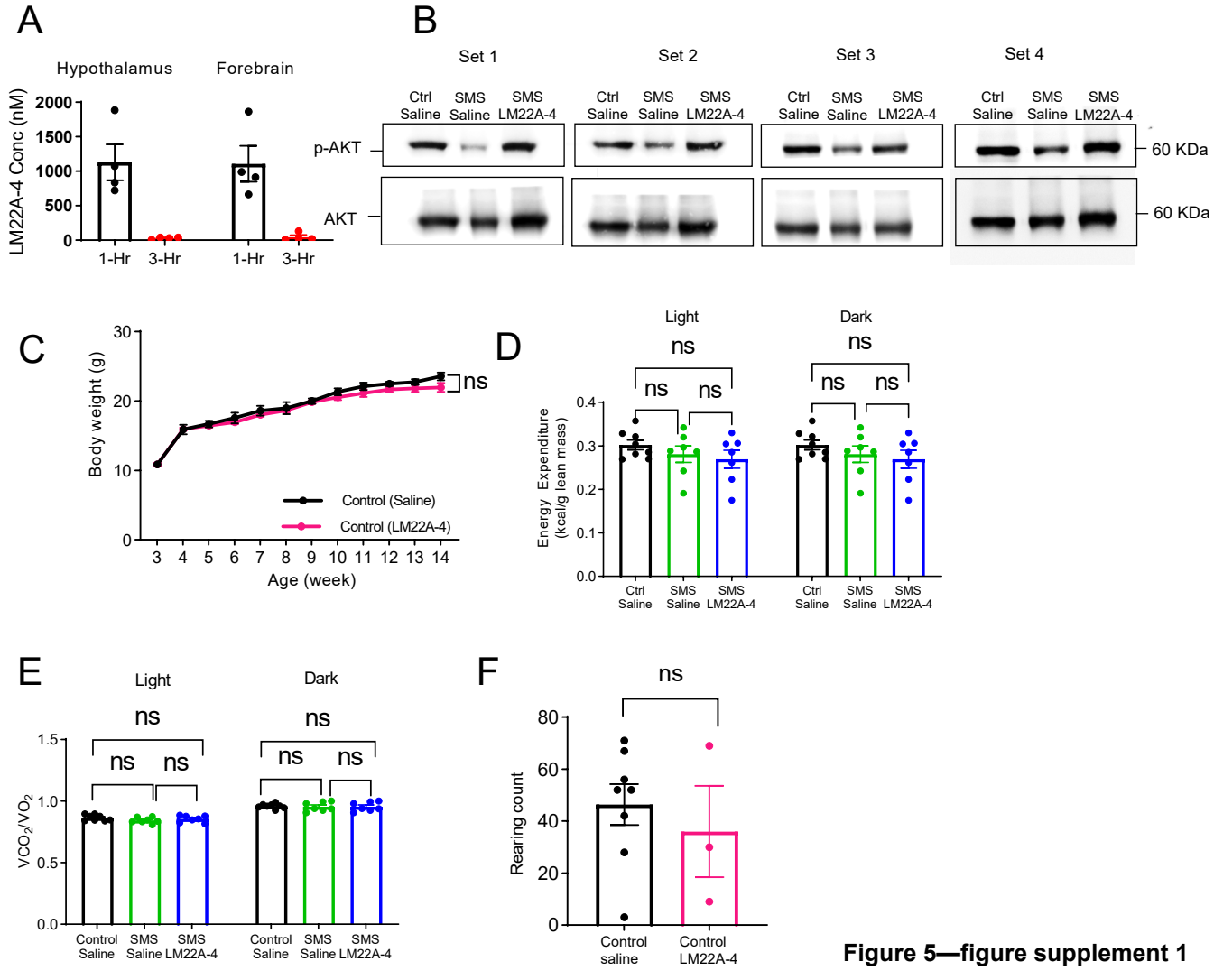

Figure 5—figure supplement 1

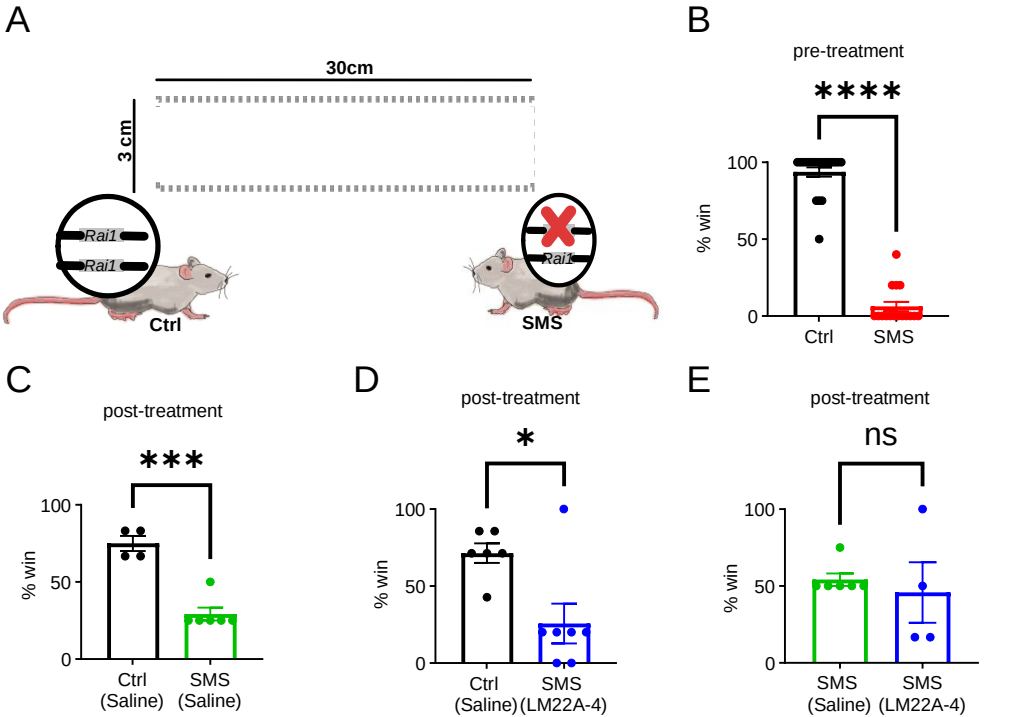

Figure 5—figure supplement 2

Uncropped western blots for staining against antibodies for P-AKT & AKT. The membrane was stripped to stain for AKT after staining for p-AKT. Before staining, the membrane was cut at band 72KDa and below 53 KDa. The yellow box represents the cropped region for images shown in this manuscript.

Set 2: Figure 5—figure supplement 1

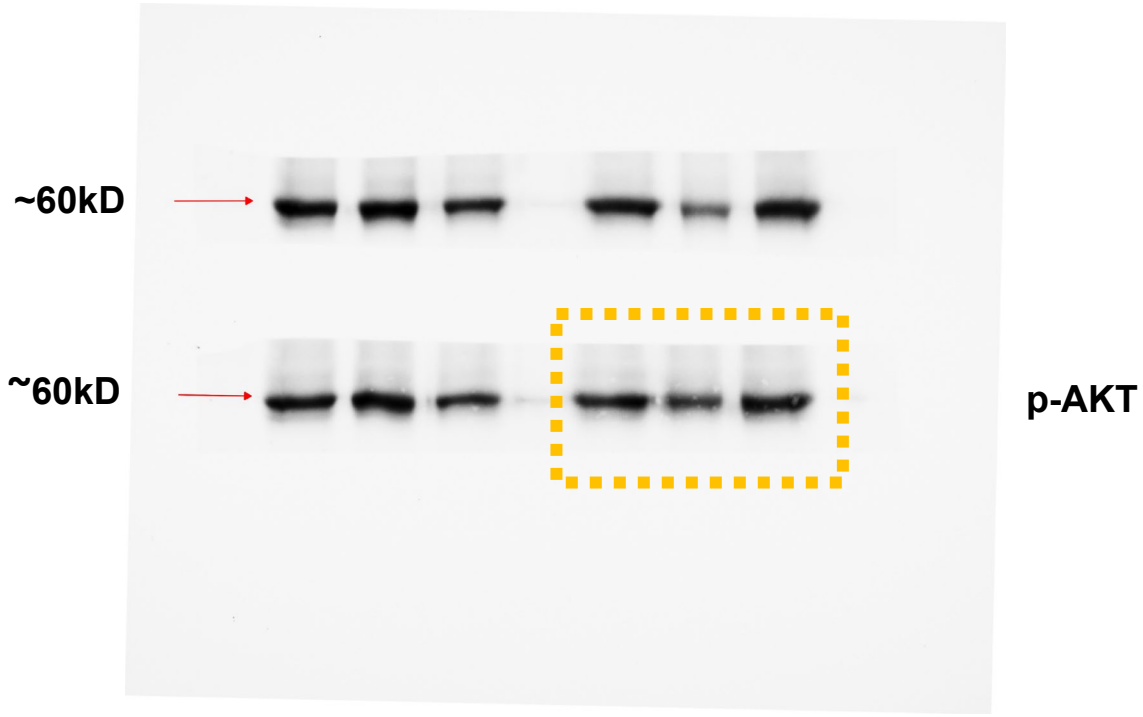

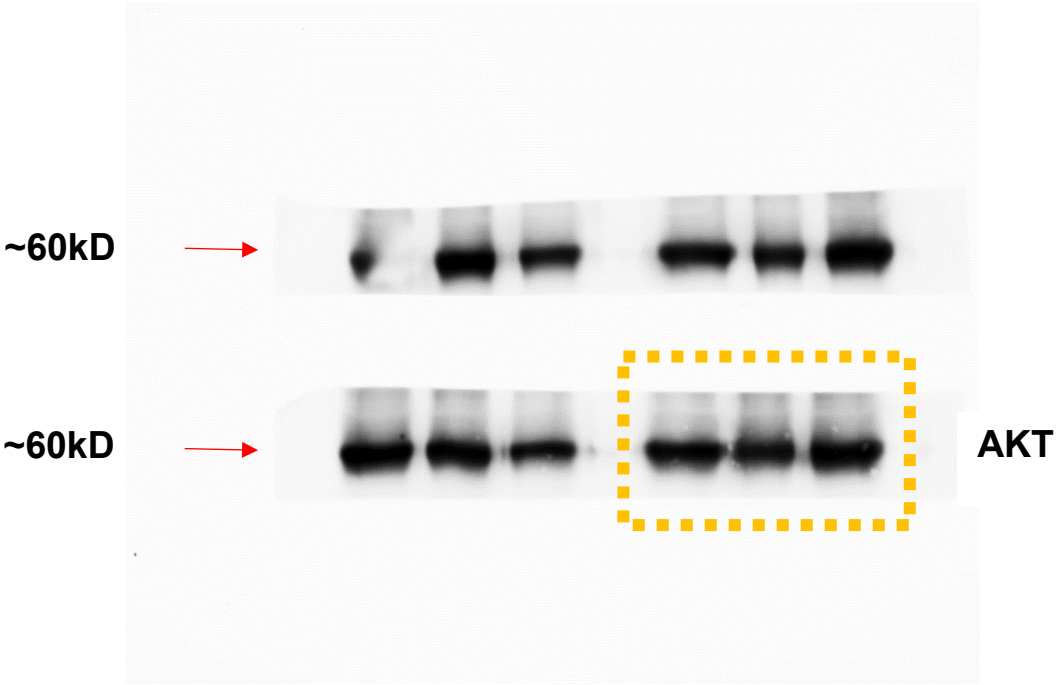

Set 4: Figure 5—figure supplement 1

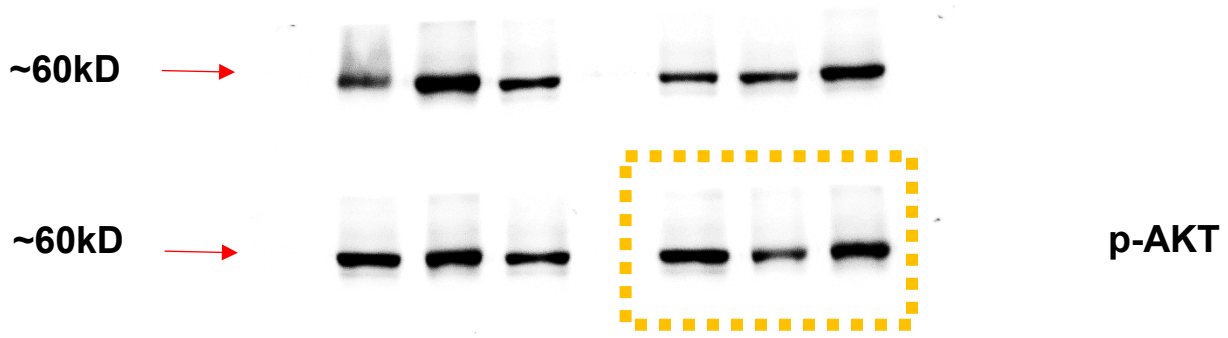

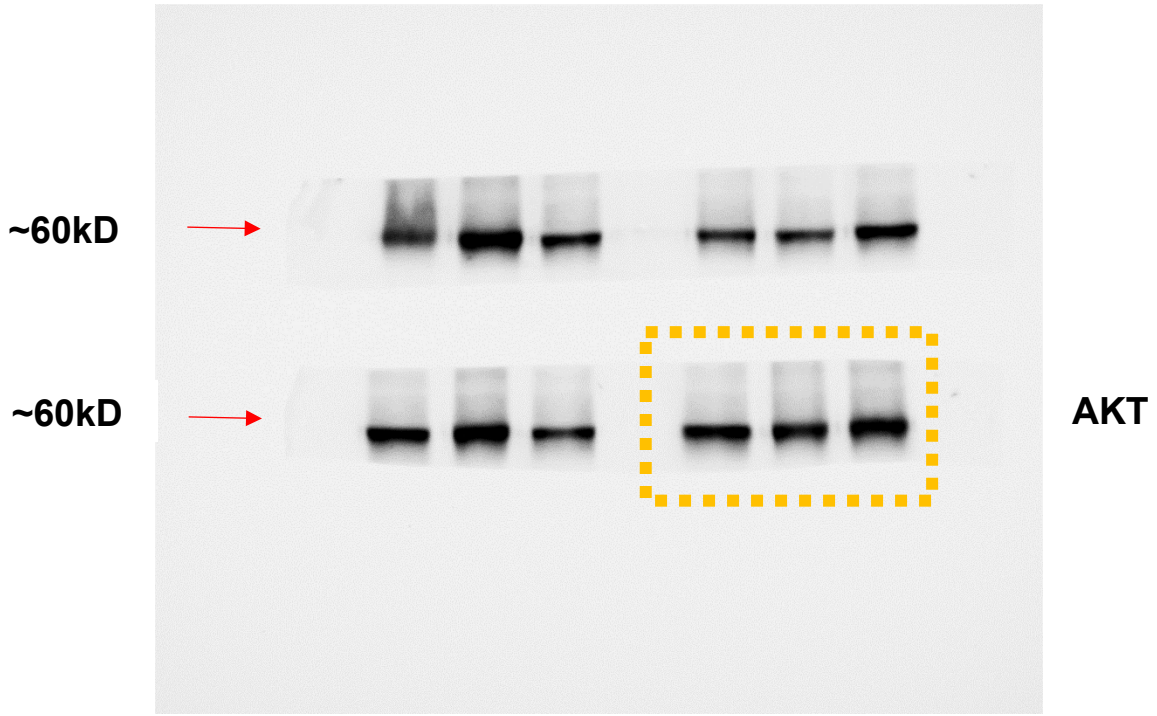

Figure 5A, same as Set 3 in Figure 5—figure supplement 1

p-AKT

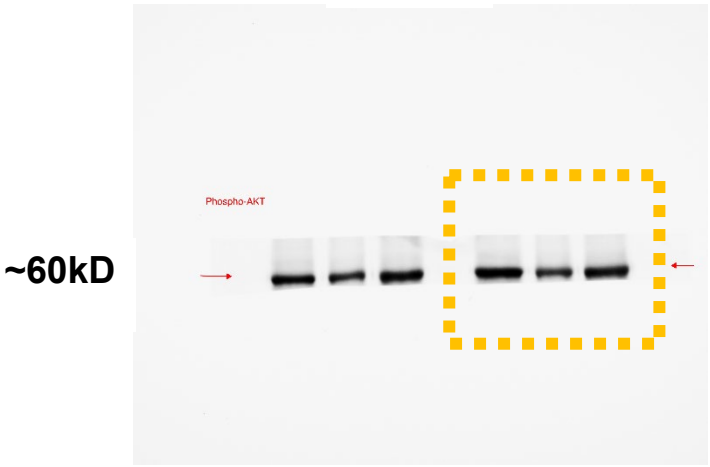

AKT

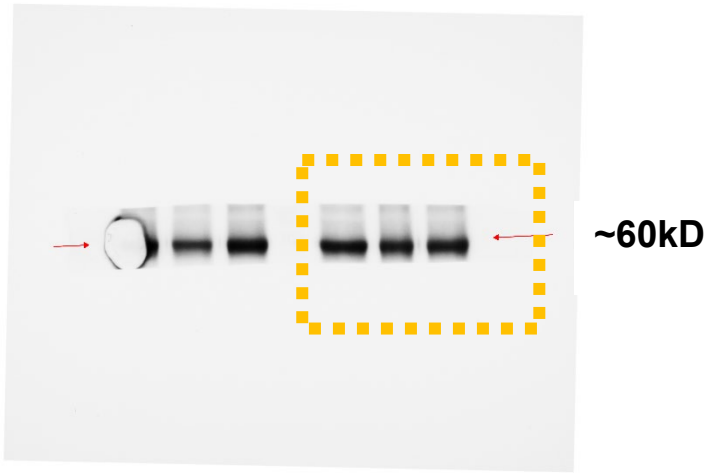

H3

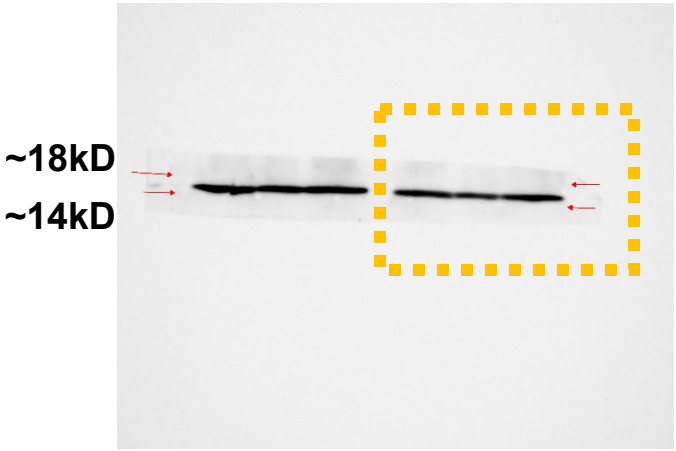

Set 1: Figure 5—figure supplement 1

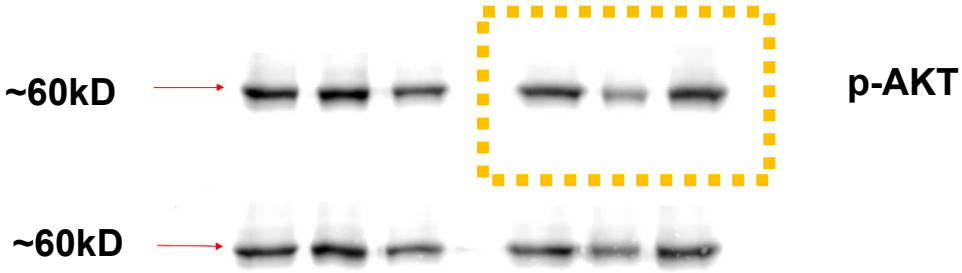

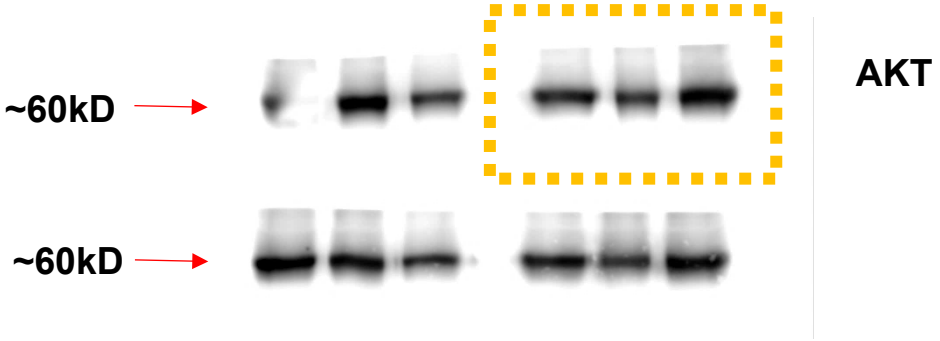
~60kD
~60kD
AKT

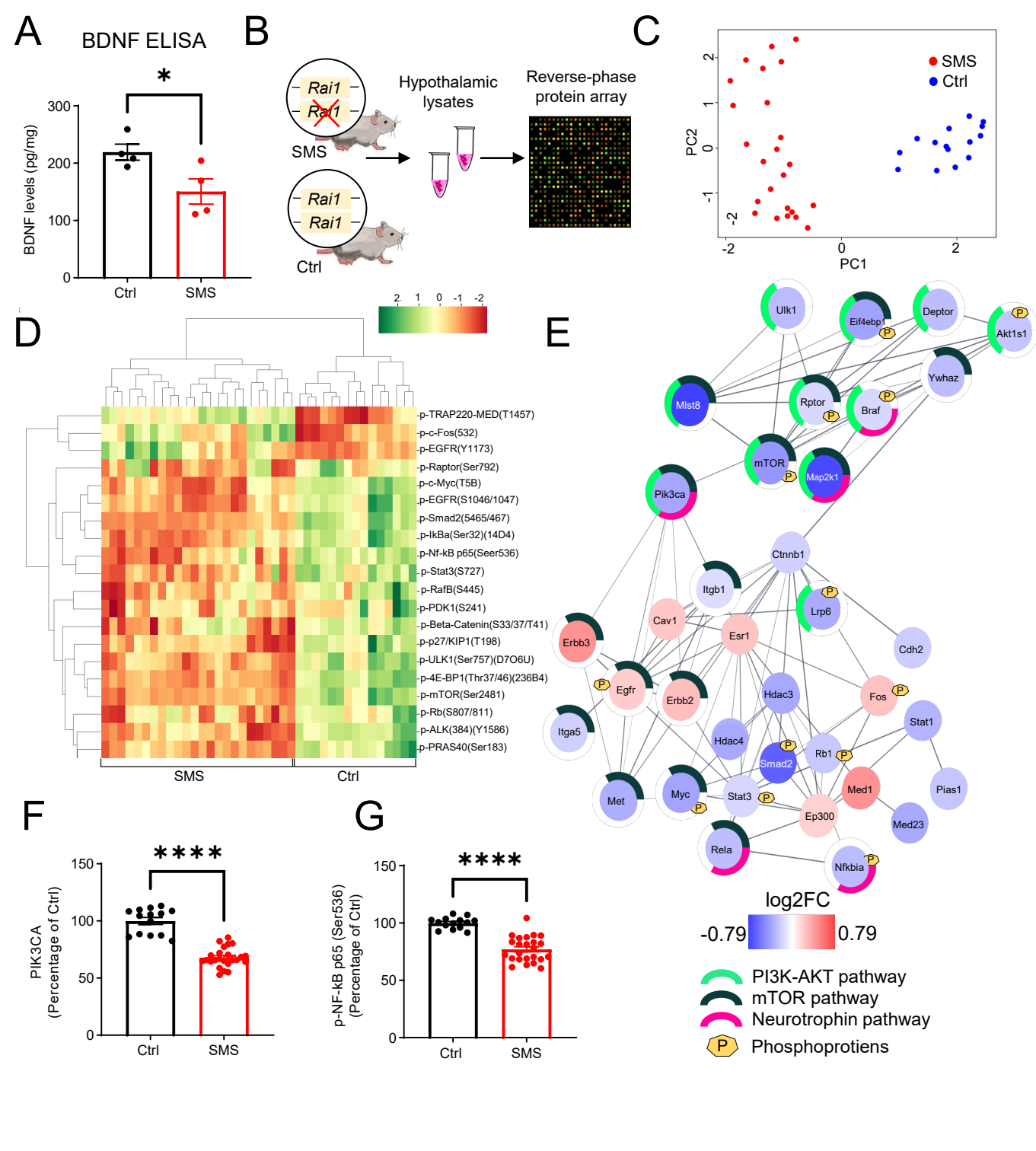
A
BDNF ELISA
*
BDNF levels (pg/mg)
300
200
100
0
Ctrl
SMS
B
Rai1
Rai1
SMS
Rai1
Rai1
Ctrl
Hypothalamic lysates
Reverse-phase protein array
C
SMS
Ctrl
PC2
PC1
2
1
0
-1
-2
D
2
1
0
-1
-2
p-TRAP220-MED(T1457)
p-c-Fos(532)
p-EGFR(Y1173)
p-Raptor(Ser792)
p-c-Myc(T5B)
p-EGFR(S1046/1047)
p-Smad2(5465/467)
p-IkBa(Ser32)(14D4)
p-Nf-kB p65(Seer536)
p-Stat3(S727)
p-RafB(S445)
p-PDK1(S241)
p-Beta-Catenin(S33/37/T41)
p-p27/KIP1(T198)
p-ULK1(Ser757)(D7O6U)
p-4E-BP1(Thr37/46)(236B4)
p-mTOR(Ser2481)
p-Rb(S807/811)
p-ALK(384)(Y1586)
p-PRAS40(Ser183)
SMS
Ctrl
E
Ulk1
Eif4ebp1
Deptor
Akt1s1
Ywhaz
Mlst8
Rptor
Braf
mTOR
Map2k1
Pik3ca
Ctnnb1
Itgb1
Lrp6
Cav1
Esr1
Erbb3
Cdh2
Egfr
Erbb2
Hdac3
Fos
Stat1
Itga5
Hdac4
Smad2
Rb1
Med1
Pias1
Met
Myc
Stat3
Ep300
Med23
Rela
Nfkbia
P
log2FC
-0.79
0.79
PI3K-AKT pathway
mTOR pathway
Neurotrophin pathway
Phosphoprotiens
F
****
PIK3CA (Percentage of Ctrl)
150
100
50
0
Ctrl
SMS
G
****
p-NF-kB p65 (Ser536) (Percentage of Ctrl)
150
100
50
0
Ctrl
SMS

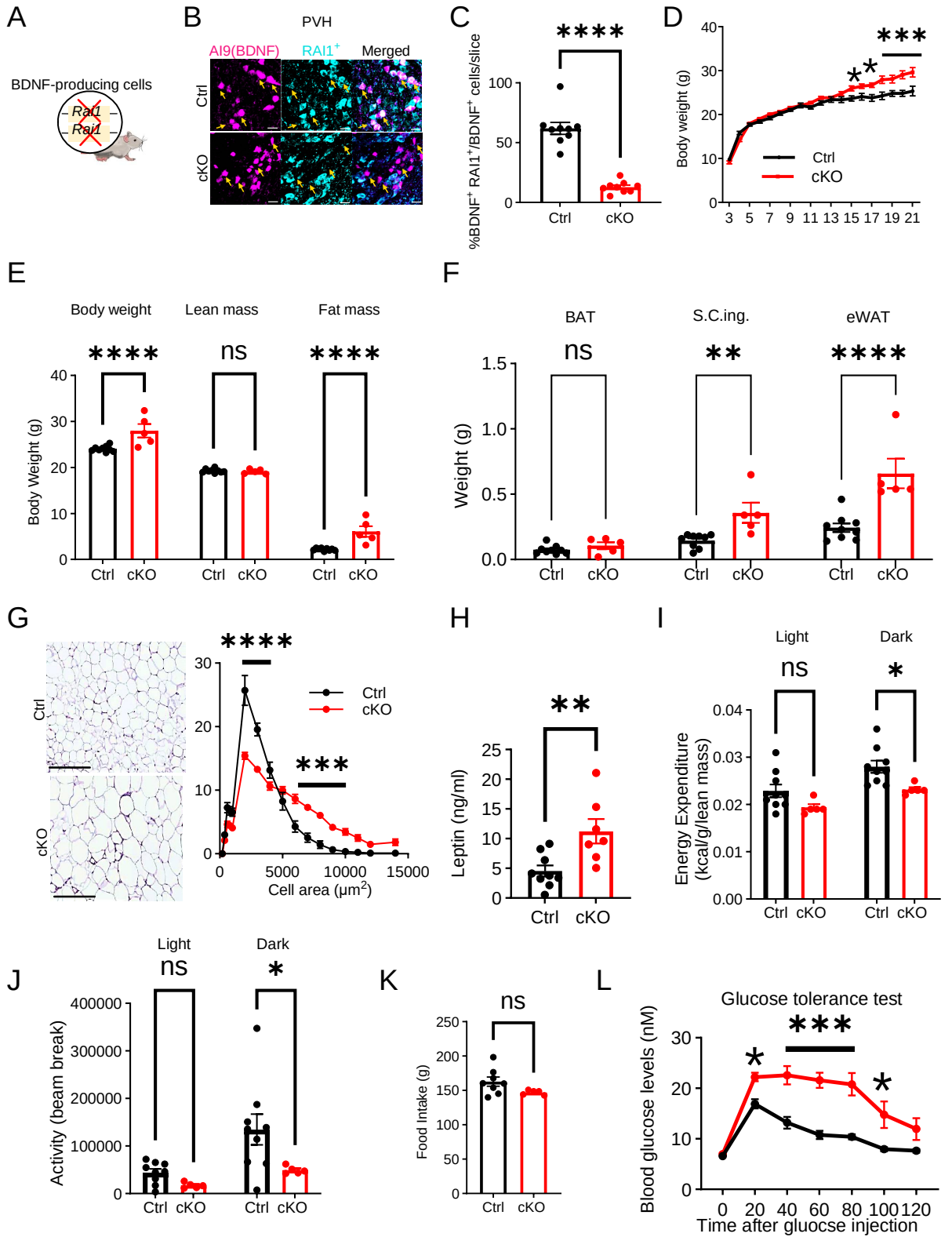
A
BDNF-producing cells
Ral1
Ral1
B
PVH
AI9(BDNF)
RAI1+
Merged
Ctrl
cKO
C
****
%BDNF+ RAI1+/BDNF+ cells/slice
100
50
0
Ctrl
cKO
D
***
**
Body weight (g)
40
30
20
10
0
Ctrl
cKO
3 5 7 9 11 13 15 17 19 21
E
Body weight
Lean mass
Fat mass
****
ns
****
Body Weight (g)
40
30
20
10
0
Ctrl cKO Ctrl cKO Ctrl cKO
F
BAT
S.C.ing.
eWAT
ns
**
****
Weight (g)
1.5
1.0
0.5
0.0
Ctrl cKO Ctrl cKO Ctrl cKO
G
Ctrl
cKO
****
***
Ctrl
cKO
30
20
10
0
0 5000 10000 15000
Cell area (μm2)
H
**
Leptin (ng/ml)
25
20
15
10
5
0
Ctrl cKO
I
Light
Dark
ns
*
Energy Expenditure (kcal/g/lean mass)
0.04
0.03
0.02
0.01
0.00
Ctrl cKO Ctrl cKO
J
Light
Dark
ns
*
Activity (beam break)
400000
300000
200000
100000
0
Ctrl cKO Ctrl cKO
K
ns
Food Intake (g)
250
200
150
100
50
0
Ctrl cKO
L
Glucose tolerance test
***
*
*
Blood glucose levels (nM)
30
20
10
0
0 20 40 60 80 100 120
Time after gluocse injection

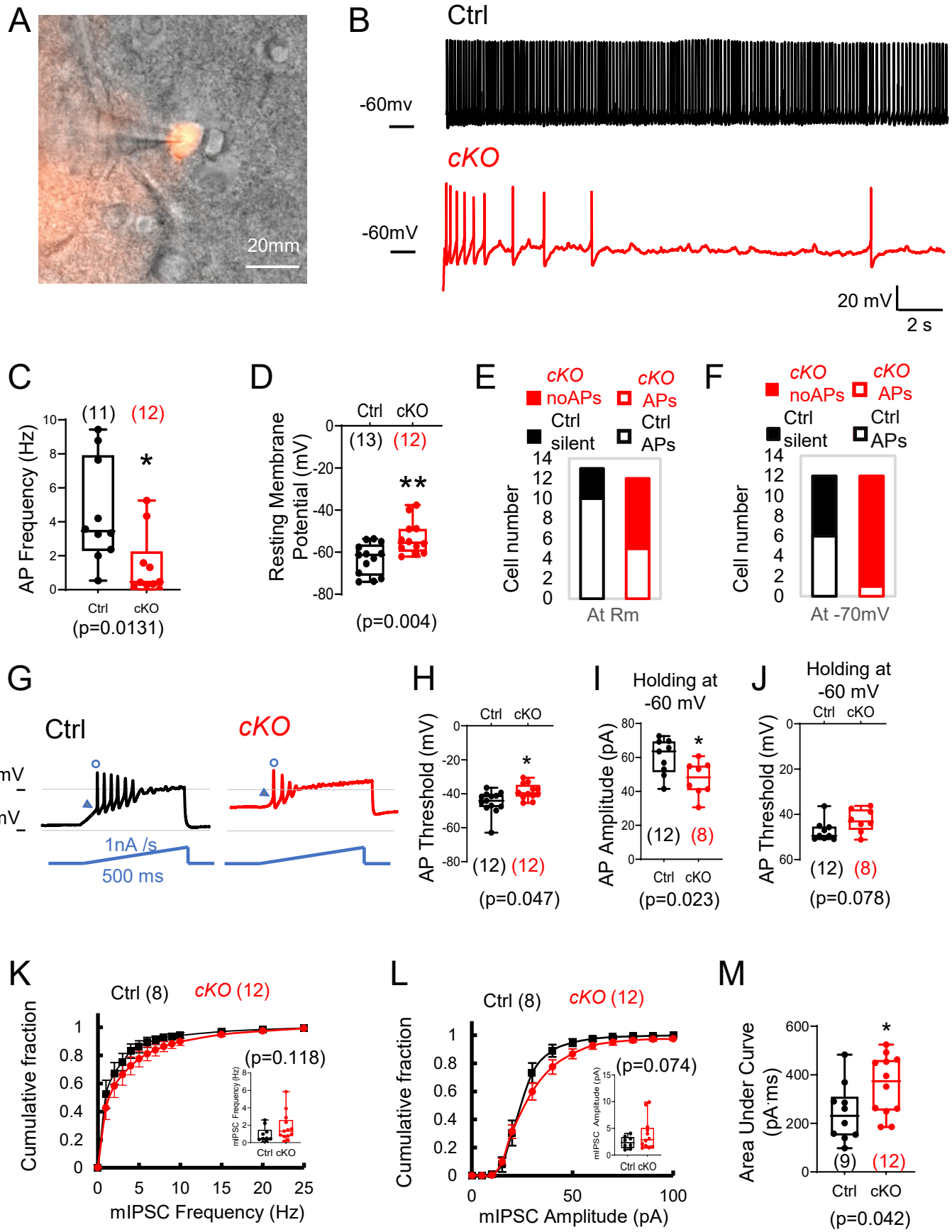
A
20mm
B
Ctrl
-60mv
cKO
-60mV
20 mV
2 s
C
AP Frequency (Hz)
(11)
(12)
*
Ctrl
cKO
(p=0.0131)
D
Resting Membrane Potential (mV)
Ctrl
cKO
(13)
(12)
**
(p=0.004)
E
cKO noAPs
cKO APs
Ctrl silent
Ctrl APs
Cell number
At Rm
F
cKO noAPs
cKO APs
Ctrl silent
Ctrl APs
Cell number
At -70mV
G
Ctrl
cKO
-40mV
-60mV
1nA /s
500 ms
H
AP Threshold (mV)
Ctrl
cKO
*
(12)
(12)
(p=0.047)
I
Holding at -60 mV
AP Amplitude (pA)
*
(12)
(8)
Ctrl
cKO
(p=0.023)
J
Holding at -60 mV
AP Threshold (mV)
Ctrl
cKO
(12)
(8)
(p=0.078)
K
Ctrl (8)
cKO (12)
Cumulative fraction
(p=0.118)
mIPSC Frequency (Hz)
L
Ctrl (8)
cKO (12)
Cumulative fraction
(p=0.074)
mIPSC Amplitude (pA)
M
Area Under Curve (pA·ms)
*
(9)
(12)
Ctrl
cKO
(p=0.042)

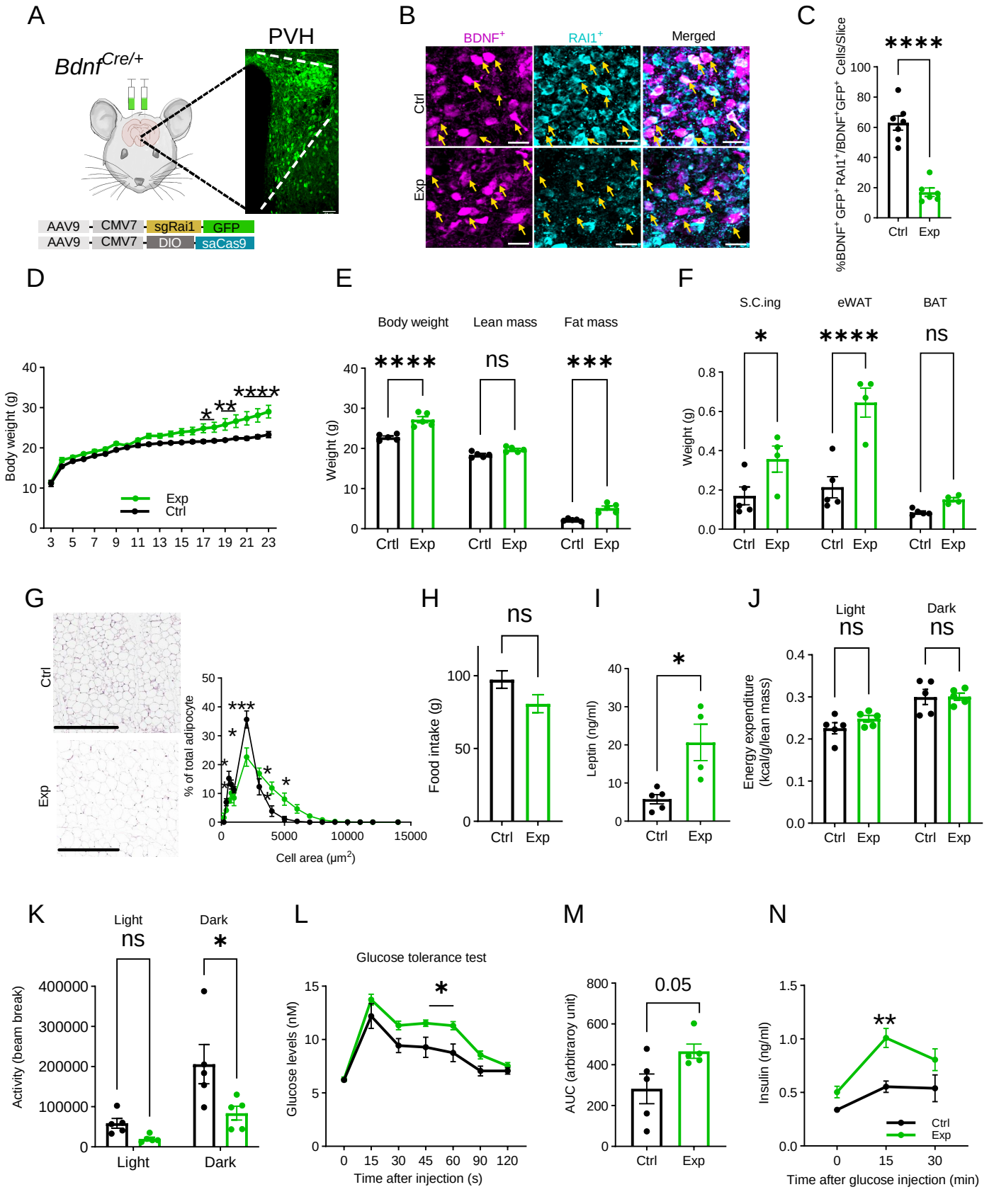
A
Bdnf Cre/+
PVH
AAV9 - CMV7 - sgRai1 - GFP
AAV9 - CMV7 - DIO - saCas9
B
BDNF+
RAI1+
Merged
Ctrl
Exp
C
%BDNF+ GFP+ RAI1+/BDNF+GFP+ Cells/Slice
****
Ctrl
Exp
D
Body weight (g)
Exp
Ctrl
E
Body weight
Lean mass
Fat mass
Weight (g)
****
ns
***
Crtl
Exp
F
S.C.ing
eWAT
BAT
Weight (g)
*
****
ns
Ctrl
Exp
G
Ctrl
Exp
% of total adipocyte
Cell area (μm2)
H
ns
Food intake (g)
I
*
Leptin (ng/ml)
J
Light
Dark
ns
ns
Energy expenditure (kcal/g/lean mass)
K
Light
Dark
ns
*
Activity (beam break)
L
Glucose tolerance test
*
Glucose levels (nM)
Time after injection (s)
M
0.05
AUC (arbitraroy unit)
N
**
Insulin (ng/ml)
Ctrl
Exp
Time after glucose injection (min)

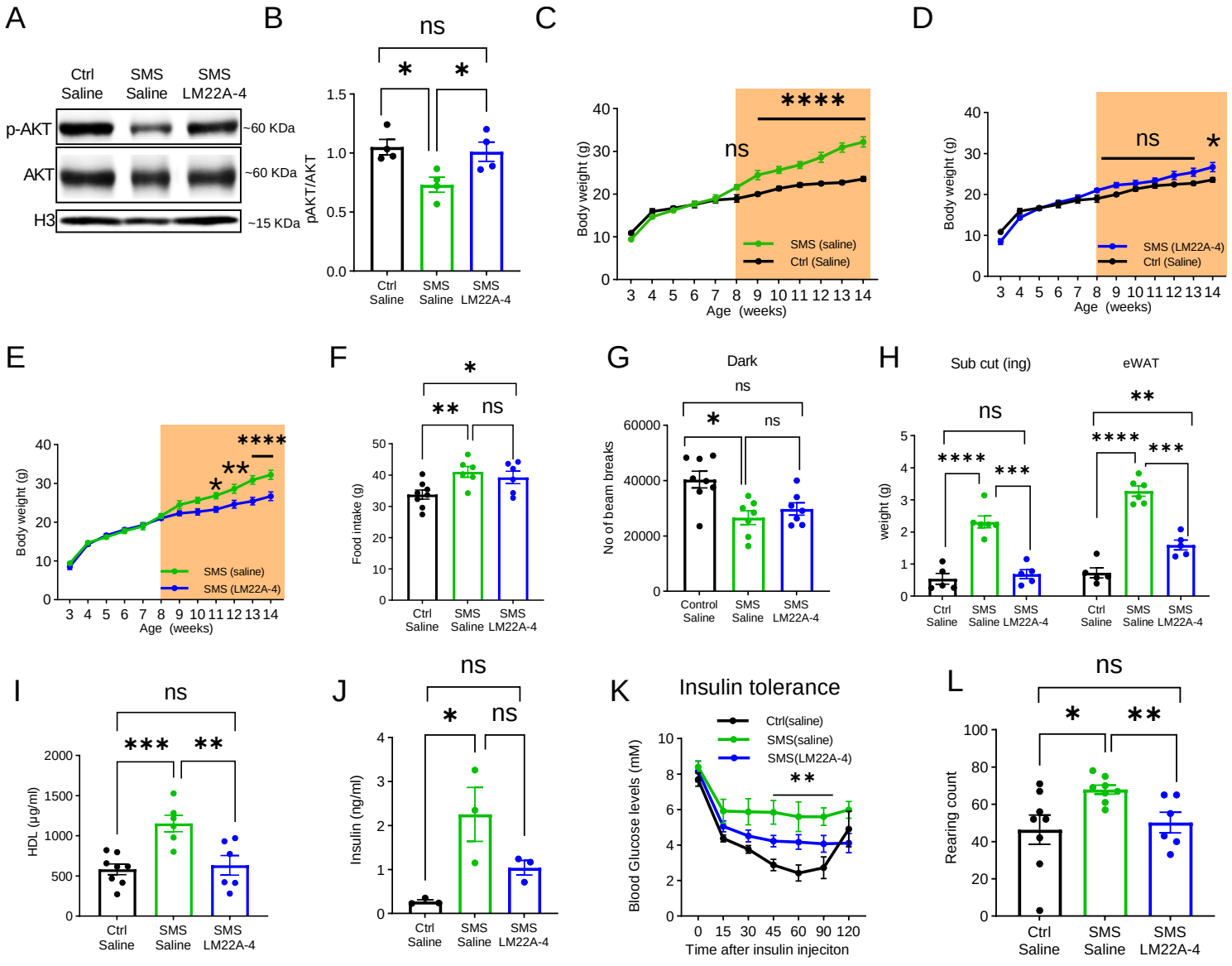
A
Ctrl Saline
SMS Saline
SMS LM22A-4
p-AKT
AKT
H3
~60 KDa
~60 KDa
~15 KDa
B
ns
*
*
pAKT/AKT
1.5
1.0
0.5
0.0
Ctrl Saline
SMS Saline
SMS LM22A-4
C
****
ns
Body weight (g)
SMS (saline)
Ctrl (Saline)
Age (weeks)
D
ns
*
Body weight (g)
SMS (LM22A-4)
Ctrl (Saline)
Age (weeks)
E
****
**
*
Body weight (g)
SMS (saline)
SMS (LM22A-4)
Age (weeks)
F
*
**
ns
Food intake (g)
Ctrl Saline
SMS Saline
SMS LM22A-4
G
Dark
ns
*
ns
No of beam breaks
Control Saline
SMS Saline
SMS LM22A-4
H
Sub cut (ing)
eWAT
ns
****
***
**
****
***
weight (g)
Ctrl Saline
SMS Saline
SMS LM22A-4
I
ns
***
**
HDL (μg/ml)
Ctrl Saline
SMS Saline
SMS LM22A-4
J
ns
*
ns
Insulin (ng/ml)
Ctrl Saline
SMS Saline
SMS LM22A-4
K
Insulin tolerance
Ctrl(saline)
SMS(saline)
SMS(LM22A-4)
**
Blood Glucose levels (mM)
Time after insulin injeciton
L
ns
*
**
Rearing count
Ctrl Saline
SMS Saline
SMS LM22A-4